UNIVERSIDADE FEDERAL DE MINAS GERAIS
School of Engineering
Graduate Program in Electrical Engineering

Rodrigo Drummond Lima

DESIGN METHODOLOGY AND OPTIMIZATION OF INTEGRATED COMMON-MODE AND DIFFERENTIAL-MODE INDUCTORS FOR POWER DRIVE SYSTEM INPUT FILTERS

Belo Horizonte
2025

Rodrigo Drummond Lima

DESIGN METHODOLOGY AND OPTIMIZATION OF INTEGRATED COMMON-MODE AND DIFFERENTIAL-MODE INDUCTORS FOR POWER DRIVE SYSTEM INPUT FILTERS

Final Version

Thesis submitted to the Graduate Program in Electrical Engineering of the Federal University of Minas Gerais in partial fulfillment of the requirements for the degree of Master in Electrical Engineering.

Advisor: Prof. Dr. Lenin Martins Ferreira Morais
Co-Advisor: Dr. Bernardo Cougo França

Belo Horizonte
2025

Lima, Rodrigo Drummond.
L732d Design methodology and optimization of integrated common-mode and differential-mode inductors for power drive system input filters [recurso eletrônico] / Rodrigo Drummond Lima. - 2025.
1 recurso online (75 f. : il., color.) : pdf.

Orientador: Lenin Martins Ferreira Morais.
Coorientador: Bernardo Cougo França.

Dissertação (mestrado) - Universidade Federal de Minas Gerais, Escola de Engenharia.

Apêndices: f. 71-75.

Bibliografia: f. 68-70.

1. Engenharia elétrica - Teses. 2. Indutores elétricos - Teses. 3. Otimização - Teses. 4. Filtros elétricos passivos - Teses. I. Morais, Lenin Martins Ferreira. II. França, Bernardo Cougo. III. Universidade Federal de Minas Gerais. Escola de Engenharia. IV. Título.

CDU: 621.3(043)

Ficha catalográfica elaborada pelo bibliotecário Reginaldo César Vital dos Santos CRB/6 2165
Biblioteca Prof. Mário Werneck, Escola de Engenharia da UFMG

UNIVERSIDADE FEDERAL DE MINAS GERAIS

ESCOLA DE ENGENHARIA

COLEGIADO DO CURSO DE GRADUAÇÃO / PÓS-GRADUAÇÃO EM ENGENHARIA ELÉTRICA

FOLHA DE APROVAÇÃO

"Design Methodology And Optimization Of Integrated Common-mode And Differential-mode Inductors For Power Drive System Input Filters"

Rodrigo Drummond Lima

Dissertação de Mestrado submetida à Banca Examinadora designada pelo Colegiado do Programa de Pós-Graduação em Engenharia Elétrica da Escola de Engenharia da Universidade Federal de Minas Gerais, como requisito para obtenção do grau de Mestre em Engenharia Elétrica.

Aprovada em 06 de fevereiro de 2025.

Por:

Prof. Dr. Lenin Martins Ferreira Morais
DELT (UFMG) - Orientador

Prof. Dr. Bernardo Cougo França
(IRT Saint Exupéry, França) - Co-orientador

Prof. Dr. Thiago Ribeiro de Oliveira
DELT (UFMG)

Prof. Dr. Porfírio Cabaleiro Cortizo
DELT (UFMG)

Dr. Hans Hoffmann Sathler
(Schaffner EMV AG - SCHAFFNER, Suiça.)

Documento assinado eletronicamente por **Lenin Martins Ferreira Morais**, **Professor do Magistério Superior**, em 06/02/2025, às 11:49, conforme horário oficial de Brasília, com fundamento no art. 5º do Decreto nº 10.543, de 13 de novembro de 2020.

Documento assinado eletronicamente por **Thiago Ribeiro de Oliveira**, **Professor do Magistério Superior**, em 06/02/2025, às 16:35, conforme horário oficial de Brasília, com fundamento no art. 5º do Decreto nº 10.543, de 13 de novembro de 2020.

Documento assinado eletronicamente por **Porfirio Cabaleiro Cortizo**, **Membro de comissão**, em 07/02/2025, às 11:10, conforme horário oficial de Brasília, com fundamento no art. 5º do Decreto nº 10.543, de 13 de novembro de 2020.

Documento assinado eletronicamente por **Bernardo Cogo França**, **Usuário Externo**, em 07/02/2025, às 12:35, conforme horário oficial de Brasília, com fundamento no art. 5º do Decreto nº 10.543, de 13 de novembro de 2020.

Documento assinado eletronicamente por **Hans Hoffmann Sathler**, **Usuário Externo**, em 11/02/2025, às 04:33, conforme horário oficial de Brasília, com fundamento no art. 5º do Decreto nº 10.543, de 13 de novembro de 2020.

A autenticidade deste documento pode ser conferida no site https://sei.ufmg.br/sei/controlador_externo.php?acao=documento_conferir&id_orgao_acesso_externo=0, informando o código verificador **3921928** e o código CRC **6AACC244**.

Referência: Processo nº 23072.206011/2025-10 SEI nº 3921928

Dedico este trabalho à minha família

Acknowledgments

First, I would like to thank my parents Angélica and Marcos, for the love, guidance and support during my academic and personal journey. To my brother Guilherme, thank you for . I extend my gratitude to my family for their continued support during this process.

To my advisor, Prof. Lenin Morais, I am profoundly grateful for your guidance and expertise. Thank you for your motivation throughout the process, and for the opportunities you provided that contributed significantly to my academic and professional growth.

To my co-advisor, Dr. Bernardo Cougo, thank you for your valuable insights and contributions to this work. Thank you also for the invitation to work at IRT Saint Exupéry, and for the reception in Toulouse.

I would also like to thank all professors from the Grupo de Eletrônica de Potência at UFMG for all the valuable teachings and dedication that made me appreciate Power Electronics.

A special thanks to my colleagues and friends from IRT Saint Exupéry, whose friendship and professional insights have added depth to my academic and personal growth.

Finally, to everyone who has been part of this journey in any capacity, thank you for your kindness, encouragement, and belief in my potential.

This work was carried out with the support of the Coordination for the Improvement of Higher Education Personnel - Brazil (CAPES) through the Academic Excellence Program (PROEX).

"*Fais de ta vie un rêve, et d'un rêve, une réalité.*"
(Antoine de Saint-Exupéry)

Resumo

Sistemas de acionamento de potência baseados em dispositivos de banda larga desempenham um papel essencial na eletrificação das indústrias de transporte. No entanto, sua implementação enfrenta muitos desafios que devem ser considerados durante o projeto, especialmente em relação à qualidade da energia no lado da rede/carga e à interferência eletromagnética (EMI). Nesse sentido, os filtros de entrada dos sistemas de acionamento de potência devem ser cuidadosamente projetados para atender aos padrões de níveis de ruído e serem otimizados em termos de peso e perdas para reduzir as emissões. Indutores são geralmente os componentes que têm o maior impacto nas perdas e no peso dos filtros de EMI e qualidade de energia. Filtros de entrada compreendem um indutor de modo comum (CM) e um indutor de modo diferencial (DM) para reduzir as emissões conduzidas e garantir a estabilidade da rede e a qualidade da energia. Este trabalho propõe um indutor integrado de CM e DM (ou indutor de Modo Duplo, *Dual-Mode* em inglês) para reduzir o peso e as perdas gerais do filtro de entrada de um sistema de acionamento de potência. A topologia proposta consiste em um indutor de CM baseado em material nanocristalino, com dois blocos de pó de ferro nas laterais para servir como um caminho alternativo para o fluxo de dispersão. Na primeira parte deste trabalho, é desenvolvido um modelo analítico preciso para o indutor de Modo Duplo, validado por simulações de método de elementos finitos tridimensionais e resultados experimentais. Em seguida, a metodologia de projeto e a rotina de otimização são apresentadas e os resultados são comparados aos de indutores discretos de CM e DM, mostrando uma redução de 20% no peso e 14% nas perdas. Por fim, um protótipo do indutor de Modo Duplo foi produzido e comparado a uma solução discreta otimizada para a mesma aplicação para validar os resultados da otimização e mostrar que a arquitetura proposta é viável para filtros de entrada.

Palavras-chave: filtros passivos; otimização de filtros; integração

Abstract

Power drive systems based on wide bandgap devices play an essential role in the electrification of transportation industry. Still, their implementation faces many challenges that must be considered during design, especially regarding power quality on the network/load side and electromagnetic interference (EMI). In that sense, input filter of power drive systems must be carefully designed to meet noise level defined on standards and be optimized in terms of weight and losses to reduce overall emissions. Inductors are usually the components that have the most significant impact on losses and weight of EMI and power quality filters. Input filters comprise a common-mode (CM) choke and a differential-mode (DM) inductor to reduce EMI conducted emissions and guarantee network stability and power quality. This work proposes an integrated CM and DM (or Dual-Mode) inductor to reduce the overall weight and losses of a power drive system's input filter. The proposed topology consists of a nanocrystalline-based CM choke with two iron powder blocks on the sides to serve as an alternative path for the leakage flux. In the first part of this work, a precise analytical model for the Dual-Mode inductor is developed, with validation by three-dimensional FEM simulations and experimental results. Subsequently, the design methodology and optimization routine are presented, and results are compared to those of discrete CM and DM inductors, showing a reduction of 20% in weight and 14% in losses. Lastly, a prototype of the Dual-Mode inductor was produced and compared to an optimized discrete solution for the same application to validate the optimization results and show that the proposed architecture is a viable solution for input filters.

Keywords: passive filters; filter optimization; integration

List of Figures

List of Tables

List of Abbreviations and Acronyms

AC	Alternate current
ALL	Adapted Leakage Layer
AR6	Sixth Assessment Report
CM	Common mode
DAB	Dual-Active Bridge
DC	Direct current
DM	Differential mode
EASA	European Union Aviation Safety Agency
ECCE	Energy Conversion Congress & Expo
EMI	Electromagnetic interference
EPE	European Conference on Power Electronics and Applications
FEA	Finite Element Analysis
FEM	Finite Element Method
GND	Ground
HF	High frequency
HFT	High-Frequency Transformers
HVDC	High-voltage direct current
IPCC	Intergovernmental Panel on Climate Change
MEA	More Electric Aircraft
ODMIS	Orthogonal Decoupling Magnetic Integrated Structure
PCB	Printed circuit board
PFC	Power factor correction
PMSM	Permanent-magnet synchronous motor
RTCA	Radio Technical Commission for Aeronautics
UFMG	Universidade Federal de Minas Gerais
VAC	*Vacuumschmelze*
WBG	Wide Bandgap
WSDOT	Washington State Department of Transportation

Contents

Chapter 1

Introduction

1.1 Context and Relevance

The Sixth Assessment Report (AR6) of the United Nations Intergovernmental Panel on Climate Change (IPCC) established that human activities have caused a global surface temperature rise of 1.1 °C in the years 2011 to 2020 in comparison to 1850 to 1900. This is mainly caused by the continuous emission of greenhouse gases that increase each year due to unsustainable energy use, lifestyles and patterns of consumption and production. The report concludes that, to avoid a warming of 1.5 °C, rapid and large-scale reductions of greenhouse gas emissions are needed (IPCC, 2023).

One of the main contributors to these greenhouse gas emissions is the aviation industry. The European Aviation Environmental Report 2022 reported full-flight CO_2 emissions of 147 million tonnes in 2019, which decreased in 2020 and 2021 due to COVID-19, but tend to reach 188 million tonnes in Europe by 2050 if no action is taken in aircraft technology. The study also shows that more electric aircraft can reduce emissions to about 59 million tonnes in conjunction with more sustainable fuels and air traffic management, as seen in Fig. 1.1 (EASA, 2022).

The aviation industry is still in the early stages of adapting to the new sustainability goals. It aims to align with the objectives of the European Green Deal, striving for net zero greenhouse gas emissions by 2050 and a 55% reduction in emissions by 2030 (European Parliament, 2024).

A way to reduce these emissions is the electrification of certain aircraft systems. More Electric Aircraft (MEA) concept consists of replacing mechanical, pneumatic and hydraulic powered systems within the aircraft with more efficient electrical power systems (WSDOT, 2019). However, this replacement faces many challenges regarding weight, losses, EMI and power quality compliances for filters.

The rising use of Wide Bandgap (WBG) technology allows higher switching frequencies, which contributes to reductions in the overall volume and weight of the system. However, noise levels become higher and thus EMI filters must be carefully designed to

Figure 1.1: Net CO_2 emissions of aircraft in Europe until 2021 and future projections for different scenarios of technology adoptions.

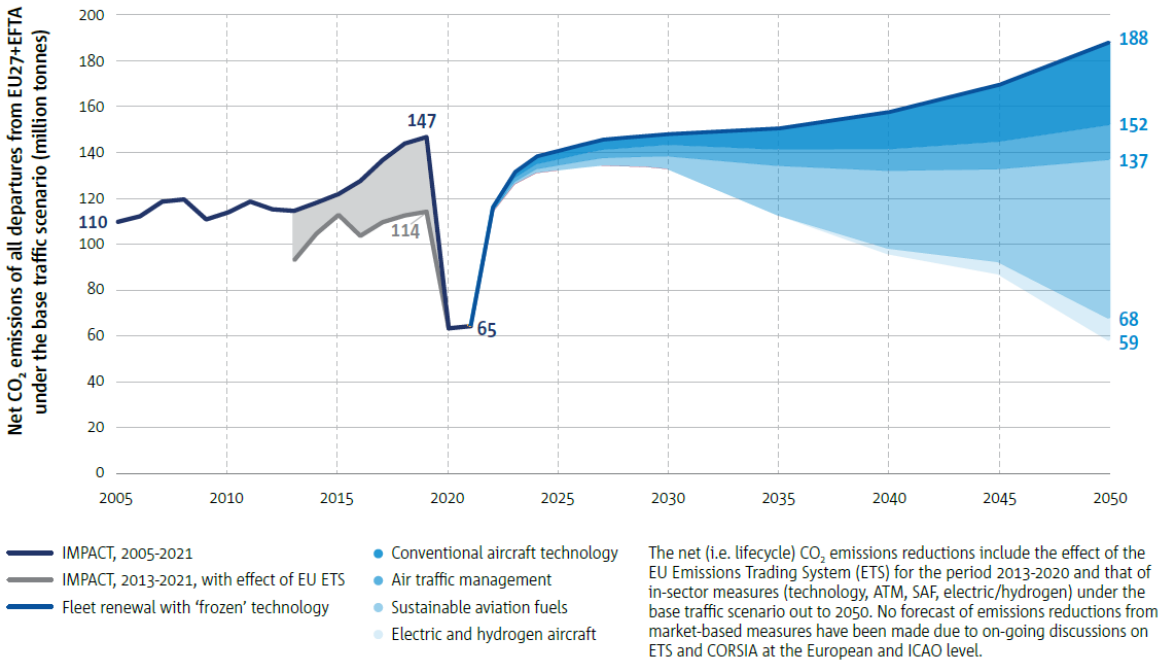

Source: EASA (2022)

meet the conducted emission standards (Zhang and Wang, 2020). In some aircraft applications, such as the one selected for this study, the Common Mode (CM) capacitor value is limited by the lightning current constraint, which leads to bulky magnetic components (Hoffmann Sathler, 2021; Lutz and Wright, 2006; Wright and Lutz, 2006). Fig. 1.2 exemplifies a power drive system highlighting the contributions of input CM and Differential Mode (DM) filters to the overall mass and losses of the system (Hoffmann Sathler, 2021).

A solution to reduce both weight and losses of EMI filters is to integrate the DM and CM inductances in the same component. This can be accomplished by adding extra magnetic paths and windings to a CM choke to increase its leakage inductance, which increases equivalent DM inductance (Cao et al., 2022).

Figure 1.2: Input EMI and Power Quality filter for aircraft applications.

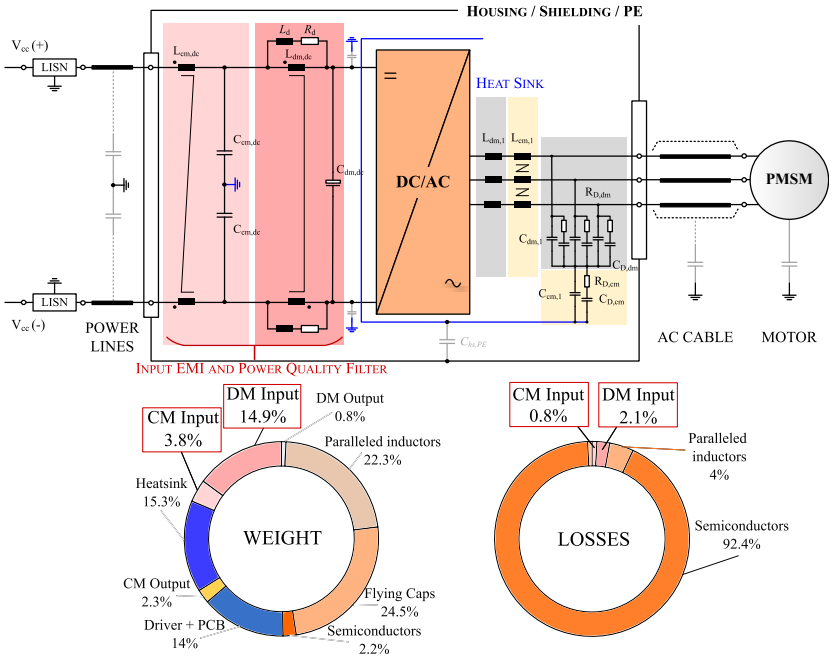

Source: adapted from Hoffmann Sathler (2021).

1.2 Objectives

1.2.1 General objective

This work aims to present an innovative solution for Power Drive Systems input filter inductors by integrating both the common-mode choke and the differential-mode inductor in the same component with the objective of reducing the overall weight and losses of the EMI and power quality filter.

1.2.2 Specific objectives

- Develop and validate a precise analytical model of the integrated CM/DM inductor;
- Use the developed model to create a design optimization routine for the Dual-Mode inductor to minimize weight and losses;
- Compare the optimal integrated inductor solutions to optimized discrete (classical)

solutions;

- Develop a prototype of an optimal Dual-Mode inductor and compare experimental results to optimization results.

1.3 Publications

The following papers have been published during the development of this thesis.

- R. Drummond, G. Almeida, B. Cougo, S. Serpaud, V. Dos Santos and L. M. F. Morais, "Modeling of Integrated CM/DM Inductors in EMI Filters for High Power Density Converters," 2024 Energy Conversion Congress & Expo Europe (ECCE Europe), Darmstadt, Germany, 2024, pp. 1-8.
- R. Drummond, B. Cougo, D. H. Tran, G. Almeida, S. Serpaud, V. Dos Santos and L. M. F. Morais, "Design Optimization of Integrated CM/DM Inductors for Power Drive Input Filter," 2025 European Conference on Power Electronics and Applications (EPE 2025), Paris, France, 2025. To be published, selected for publication in the EPE'25 special issue of "Power Electronic Devices and Components" journal.

1.4 Thesis Structure

This work is structured as follows:

- In Chapter 2, we provide an overview of the input filters used in Power Drive Systems, emphasizing the main constraints and objectives associated with each stage of the filter. Additionally, we conduct a comparative analysis of magnetic materials, discussing the most suitable materials for common-mode (CM) and differential-mode (DM) components.
- Chapter 3 presents the state of the art, covering literature about high leakage inductance magnetic components in several applications on Power Electronics, as well as the advancements of its use in EMI filters. An overview of magnetic component optimization is also provided.

- In Chapter 4, a topology for the Dual-Mode inductor is chosen and precise analytical models for CM and DM configurations are developed and validated by experimental results.
- In Chapter 5, a design optimization routine is presented, as well as a deeper analysis of parameter sensibility and impact on optimization results.
- In Chapter 6, the analytical model developed in Chapter 4 is validated by experimental and simulation results. Additionally, a case study is developed for a 50kW Power Drive System input filter, in which a prototype for the optimized Dual-Mode inductor is compared to an optimized pair of CM choke and DM inductor for the same application.
- Finally, in Chapter 7, conclusions and continuity proposals of this work are presented.

Chapter 2

Background

This chapter will discuss the main concepts regarding the development and optimization of a Dual-Mode inductor. First, the input filters of Power Drive Systems will be presented. DM and CM parts will be discussed as well as the constraints regarding the design of these filters. Afterwards, a review of magnetic materials will be made, emphasizing the main characteristics of each material that can enhance the performance of the Dual-Mode inductor.

2.1 Input filters of Power Drive Systems

The input filters of Power Drive Systems for aircraft are the interface between the converter and the aircraft HVDC network. This DC bus has high demand of power quality and stability, therefore the Power Drive System has to meet requirements of maximum current and voltage ripple and input impedance, besides the noise levels of the standard RTCA DO-160G for conducted emissions. The differential-mode filter is generally composed by a DM inductor, a capacitor and a damping circuit (Dos Santos, 2019). Fig. 2.1 depicts some of the possible topologies.

Figure 2.1: DM input filter topologies.

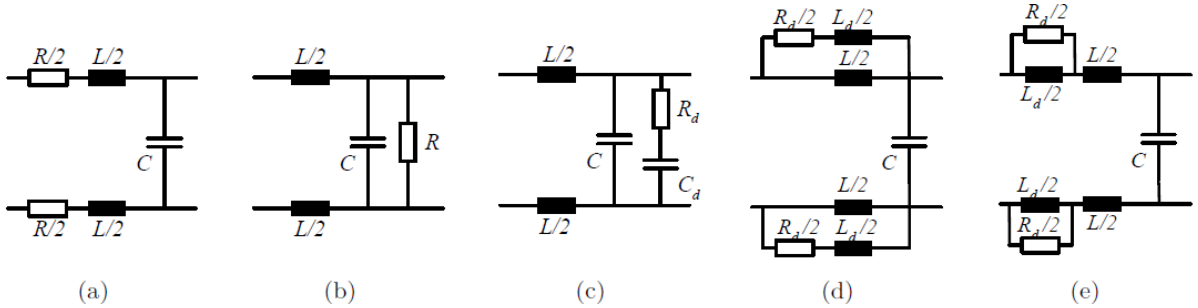

Source: Dos Santos (2019).

The main objective of this filter is to absorb harmonics emitted by the converter

or other elements connected to the network. The damping circuit serves to mitigate the resonance between the inductor and the capacitor of the filter and avoid noise amplification at the resonace frequency of the filter. The DM inductor can be made with gaped ferrite or iron powder cores. Iron powder cores are often a better choice because they have higher saturation flux density and distributed air gap, leading to more compact designs and lower fringing flux. Fig. 2.2 represents a typical standards for network stability of aircraft systems.

Figure 2.2: Power quality and network stability exigences for avionic systems.

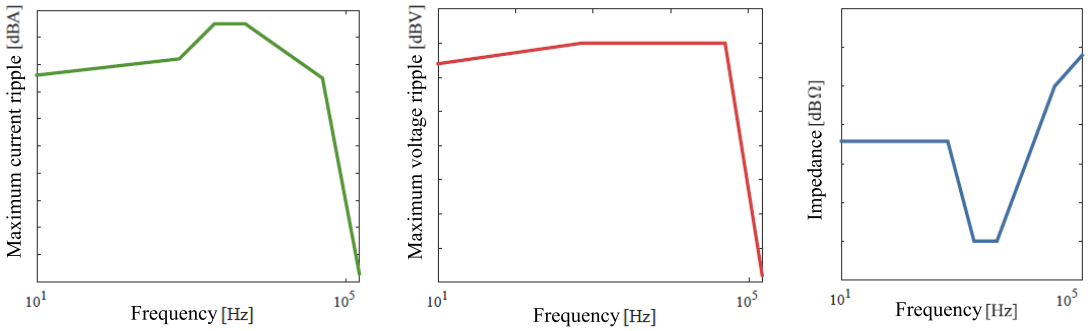

Source: Dos Santos (2019).

For common-mode, the EMI filter comprises a common-mode choke and capacitors connected to ground (GND). For aircraft applications, the capacitor value has a value limitation of 150 nF due to the lightning current constraint WF5A – DO 160G (Hoffmann Sathler, 2021). In that regard, the CM inductance reaches high values because the capacitor contribution to noise mitigation is very low due to the low capacitance. Therefore, the use of high permeability materials in CM chokes is desirable to avoid high number of turns, which can lead to high copper losses and parasitic capacitances between windings that reduce filter performance (Sclocchi, 2010). The input Conducted Emissions (CE) standards for avionics RTCA DO-160G can be seen in Fig. 2.3.

Figure 2.3: Maximum Level of Conducted Emissions RTCA - DO-160G - Category L, M & H for Power Lines.

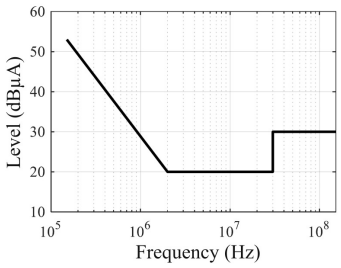

Source: Hoffmann Sathler (2021).

2.2 Magnetic Materials

Magnetic materials used in Power Electronics have very different characteristics that can impact the design of an inductive component. In this work, the material choice is very important since the integrated inductor must have good performance in differential and common modes, which have distinct requirements for current amplitude and frequency range. Beyond that, the use of these materials can be mixed within the design parts and the interactions between them must be taken into account. In this context, the main magnetic materials are compared in the graph of Fig. 2.4 (Rylko et al., 2009).

Figure 2.4: Graphical comparison of various magnetic materials.

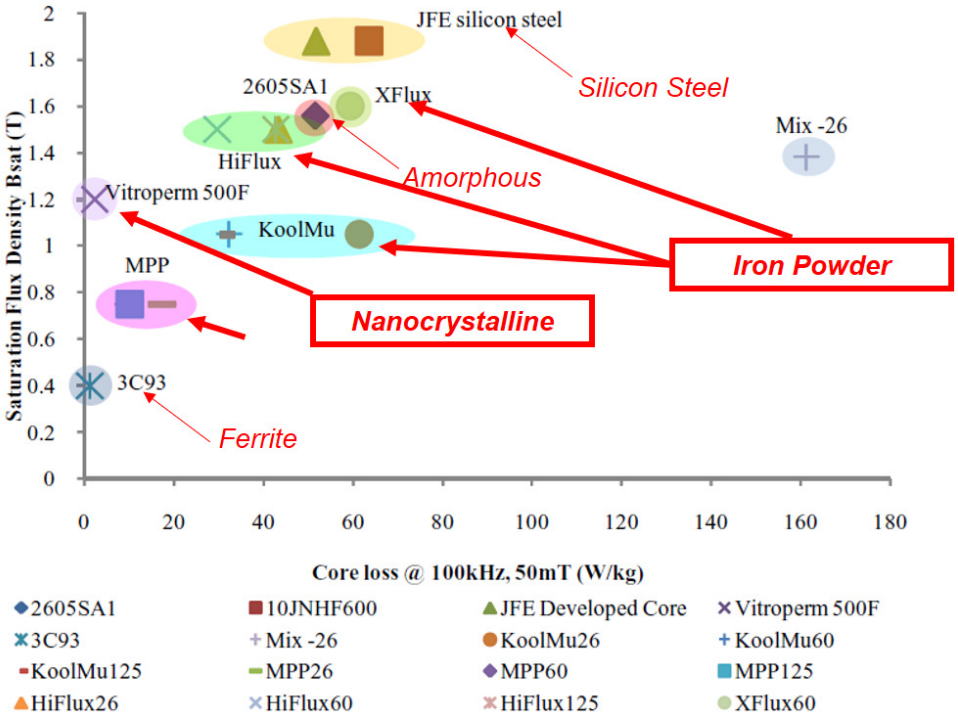

Source: adapted from Rylko et al. (2009).

The graph shows that ferrite and nanocrystalline materials have lower losses at high frequency. However, nanocrystalline cores have higher saturation flux density, which allows less usage of magnetic materials, leading to lighter and more compact designs.

Nevertheless, ferrites are low-price magnetic materials with a suitable fabrication process, allowing its parts to be molded into diverse geometries, making them usable for applications that demand non conventional geometry (Magnetics-Inc., 2021). Ferrite cores also have good thermal conductivity compared to other magnetic materials (3.5 to 5 W/m K), making it a good option for high-frequency high-power applications. Additionally, the fact that it has a low saturation flux density, from 0.3 to 0.5 T, lead to bulky components that have great contact area to dissipate heat (Rodriguez-Sotelo et al., 2020; Kacki et al.,

2017).

On the other side, nanocrystalline tape-wound cores are composed of extremely thin tapes, with each ribbon exhibiting a thickness of approximately 20 µm. In that sense, this material is most likely available in toroidal shapes. A notable advantage of the nanocrystalline over ferrite and certain iron powder cores is its high saturation flux density, which reaches 1.2 T (Vacuumschmelze, 2016; Rodriguez-Sotelo et al., 2020; Kacki et al., 2017).

This material typically exhibits high permeability, ranging from 15,000 to 200,000 (Vitroperm 500F and Nanoperm), though it is also available in lower values, ranging from 200 to 6000 (Vitroperm 250F, Nanoperm, and kμ). In this context, the lower permeability ones have the advantage of a higher cutoff frequency value due to skin effect, but need a higher number of turns to achieve the same inductance value (Bashar et al., 2016; Kacki et al., 2017).

Nanocrystalline cores are the most suitable choice for the common-mode part of the integrated inductor, since they have good behaviour at high frequencies, low losses and high saturation flux density, allowing for lighter and more compact solutions.

For differential mode, the best choices are usually iron powder materials because they have very high saturation flux density and low losses at low frequency. Additionally, they have distributed air gap, which reduces the fringing flux and reduce the permeability variation slope with field intensity, avoiding aggressive saturation current spikes.

2.3 Chapter Conclusions

This chapter discussed the importance of Power Drive input filters for ensuring network stability and compliance with CE in aircraft applications. Additionally, it compared the primary magnetic materials used in Power Electronics, identifying the most suitable options for each type of filter inductor: nanocrystalline material for the common-mode choke and iron powder for the differential-mode inductor.

Chapter 3

State of the Art

In this work, the main objective is to present a design methodology for integrated common-mode and differential-mode inductors. A way to achieve a magnetic component with relevant CM and DM inductances is by increasing the leakage inductance of a CM choke. In that sense, several ways to increase leakage inductance of magnetics were proposed in the literature for High-Frequency Transformers (HFT) of resonant converters and for Common-Mode Chokes (2 and 3-phase cases). This chapter will analyze the different proposed methods to increase the leakage inductance of a magnetic component and select the most efficient for weight and loss reduction.

3.1 Magnetics with high leakage inductance

The most efficient methods to increase leakage inductance consist of adding extra magnetic paths called Leakage Layers, and can be done in various ways (Pavlovsky et al., 2006; Cougo and Kolar, 2012; Cao et al., 2022; Wang et al., 2019). High leakage inductance integration can be found in some high-frequency transformer (HFT) applications for isolated DC-DC converters. In Cao et al. (2022), several structures of increased leakage inductance are compared in a transformer for Dual-Active-Bridge (DAB) converters using amorphous tape-wound cores and ferrite. The evaluated structures can be seen in Fig. 3.1.

Results from the structure in Fig. 3.1(a) show reductions in weight and volume compared to discrete magnetic parts (b) and no change in losses, resulting in a power density increase. This structure is also more efficient than the other high leakage configurations in (c) and (d).

Cougo and Kolar (2012) discuss using leakage layers in tape-wound cores for HF transformers. They conclude that these magnetic paths must be adapted to the geometry of tape wound cores so that the leakage flux does not flow through the tape-wound core ribbons perpendicularly so that the area is too high. Consequently, eddy currents increase,

Figure 3.1: High leakage inductance structures for HFTs. (a) Orthogonal Decoupling Magnetic Integrated Structure (ODMIS). (b) Discrete magnetic parts. (c) Large leakage inductance integrated structure. (d) Decoupling integrated structure (Gao and Zhao, 2021).

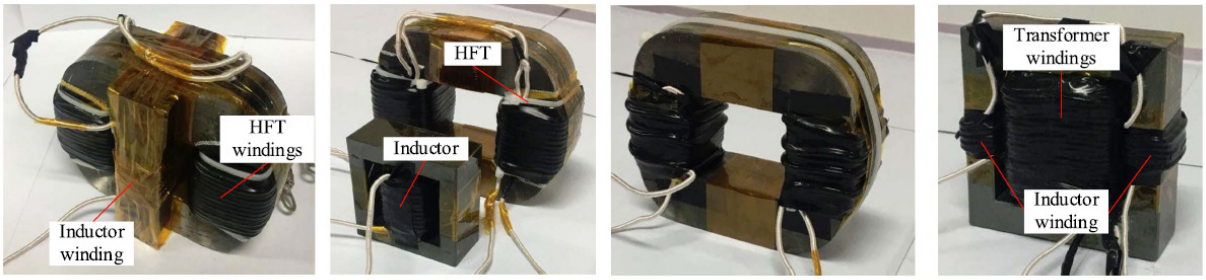

Source: Cao et al. (2022).

as well as the losses. In that sense, the authors propose Adapted Leakage Layer topologies always to have magnetic flux tangential to the ribbons. These topologies can be seen in Fig. 3.2.

Figure 3.2: Adapted leakage layer structures. (a) Extra outside core. (b) Extra core inside main window. (c) Between two core halves. (d) Outside legs on the sides.

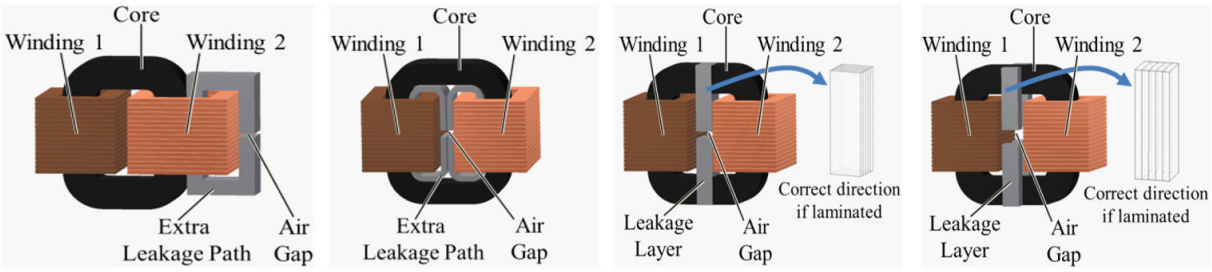

Source: Cougo and Kolar (2012).

The extra outside core topology (3.2(a)) is not ideal for EMI filters since it is not symmetric, which can lead to conversion of CM noise to DM. The extra core inside main window (3.2(b)), although being symmetric, has high fabrication complexity and increases winding perimeter, which can increase copper losses. The leakage layer between two nanocrystalline core halves (3.2(c)) is compact, but has DM and CM fluxes flowing through the leakage layer block, which facilitates its saturation. Another disadvantage is the fact that the nanocrystalline ribbons are cut, forming short circuits where the flux flows perpendicularly, which could increase eddy currents and losses. The topology with outside legs on the sides of the nanocrystalline core is the most adequate because of its symmetry and compactness. In addition, the leakage layer only has DM flux, enabling the use of iron powder cores.

3.1.1 Application in EMI filters

Magnetic integration of CM/DM chokes in EMI filters has been explored by several authors. Chen et al. (2008) published a patent for dual-mode inductors topologies that enhance differential-mode inductance but they do not specify materials nor particularities involving them. They also do not propose extra windings on the leakage paths to increase the DM inductance. As seen in Fig. 3.3, the patent also proposes a break on the structure, which can reduce significantly the magnetizing inductance of the component.

Figure 3.3: Dual-mode inductor topology proposed by Chen et al. (2008).

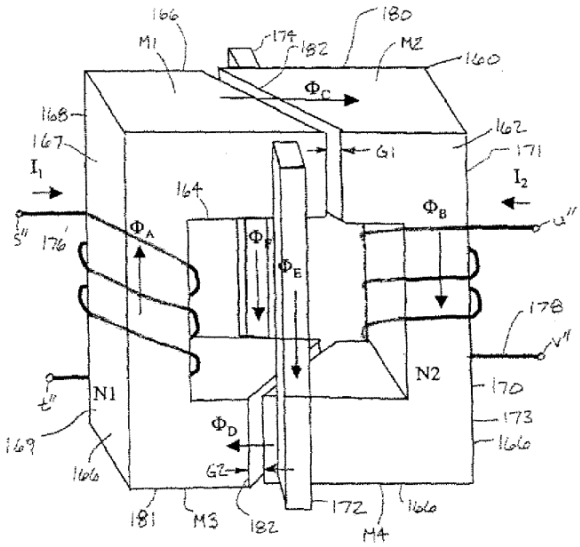

Source: Chen et al. (2008).

Other two patents for integrated inductors were published by Upadhyay (1994) and Shudarek (2009), which drawings can be seen in Fig. 3.4. In (a), a gapped EI core with ferrite is proposed and the windings are localized on the I-core. This solution can lead to low CM inductance due to the air gaps in the common-mode flux paths, which results in high reluctance. In (b), the solution is for a three-phase application, but does not have air-gaps for the common-mode, only for differential-mode. The downside is that it uses ferrite or powdered iron for both CM and DM flux paths, as the core pieces have to be from the same homogeneous material, leading to an unoptimized design and bulky components.

Tan et al. (2013) uses EQ ferrite cores as magnetic paths to the differential-mode flux of toroidal nanocrystalline CM choke but presents low increase of DM inductance and high weight due to the use of ferrite, unoptimized geometry, and high air-gap length, as seen in Fig. 3.5.

Singh et al. (2024) propose integrating ferrite toroidal chokes with ER and I blocks.

Figure 3.4: Integrated inductors patent proposals. (a) Using an EI type core with air gaps and windings on the I-core. (b) Three phase integrated inductor with homogeneous magnetic material core.

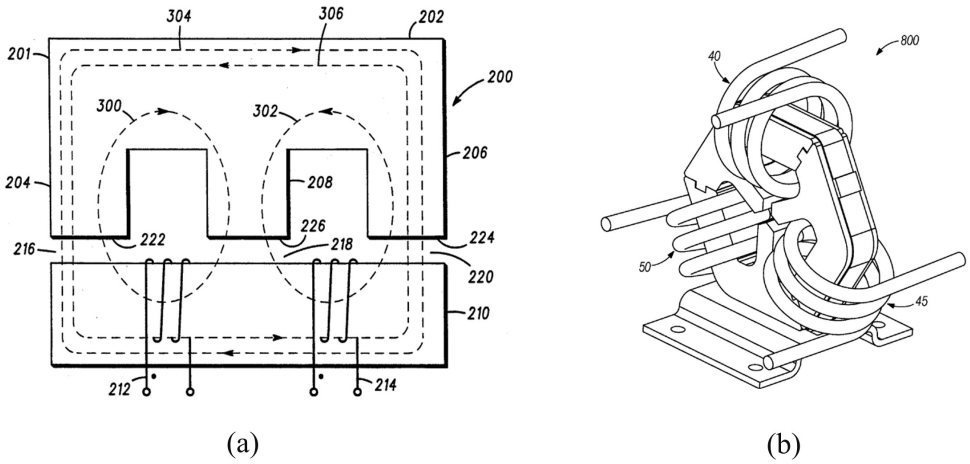

(a) (b)

Source: (a)Upadhyay (1994), (b)Shudarek (2009).

Figure 3.5: Integrated inductor structure with EQ core and toroidal CM choke. (a) and (c) top view, (b) and (d) front view.

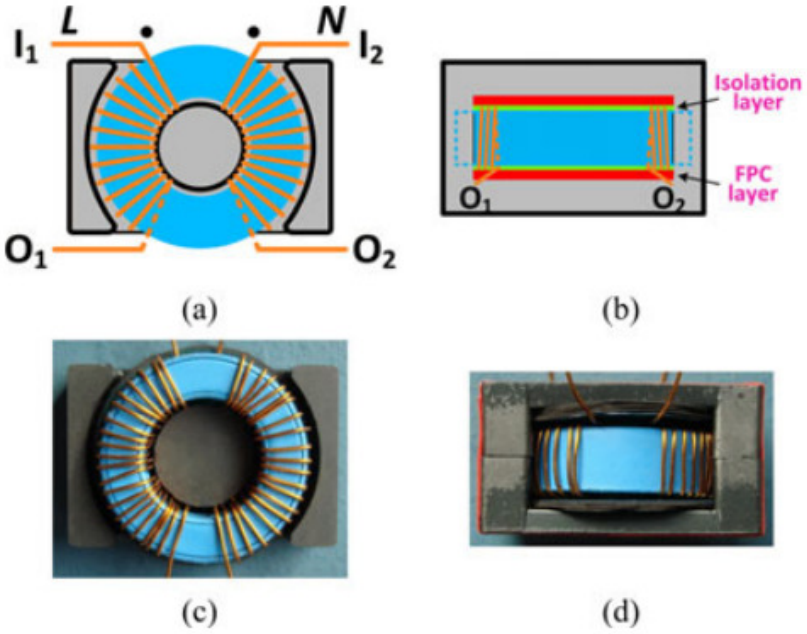

Source: Tan et al. (2013).

The work shows that this core arrangement reduced PCB area, but the weight remained the same. Further studies by Lai et al. (2010) and Borsalani et al. (2021) (Fig. 3.6 (a) and (b)) introduce new structures using ferrite cores, showing reductions in volume and copper wire length, but they still rely on ferrite, which is not the most optimized material for high performance in terms of weight, volume, and losses (Nikolov and Valchev, 2009). However, these two structures use windings on the leakage paths to add extra differential-mode inductance, which make them more compact for higher required inductances.

Figure 3.6: (a) Integrated inductor structure with two ferrite toroids. (b) Integrated inductor with a main window wound I-core.

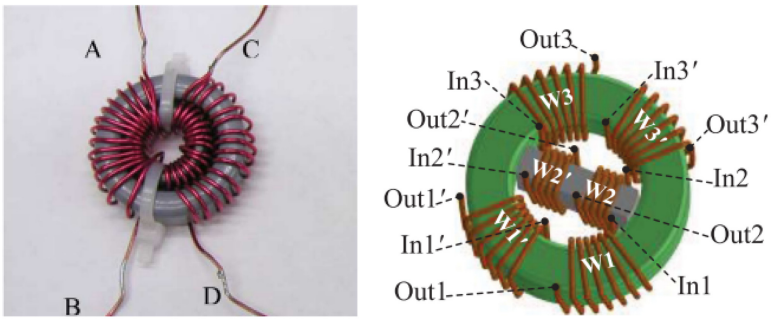

(a) (b)

Source: (a) Lai et al. (2010), (b) Borsalani et al. (2021).

Nevertheless, none of these works optimize the dual-mode inductor to perform better than an optimized traditional discrete solution. To achieve that, the core must use nanocrystalline material because of the high saturation flux density and good behavior at high frequency. However, tape-wound cores present constraints linked to the magnetic flux inside its layers. If the flux flows orthogonally through the layers, the eddy currents become very high, increasing the losses. In that regard, it is important to make adaptations to the leakage layers, as what was done by Cougo and Kolar (2012), so that the constraints and singularities of adding extra magnetic paths to tape-wound cores are adressed and losses remain at low levels.

3.2 Optimization of Magnetic Components

Several works regarding magnetics design optimization on both system-level and component-level have been developed. Mühlethaler (2012) developed a system optimization for three-phase PFC rectifier, and, in order to optimize the input filter inductor, core loss, winding loss and thermal models had to be developed. This is due to the fact that the flux waveform on the inductor is sinusoidal with a high-frequency ripple, as shown in Fig. 3.7. In that regard, all these models are needed to design an optimal magnetic component because the main design constraint is the temperature rise of the inductor.

In the case of this work, the inductor has a high DC current with low-amplitude low-frequency ripples (<5%) on the DC bus for the differential-mode and also low-amplitude high-frequency oscilations for the common-mode. Therefore, no core loss nor HF winding loss will be developed. Temperature is then not a main issue in this design since iron losses are low due to DC current and copper losses are mainly on the DC

Figure 3.7: Different flux waveforms and their B-H loops.

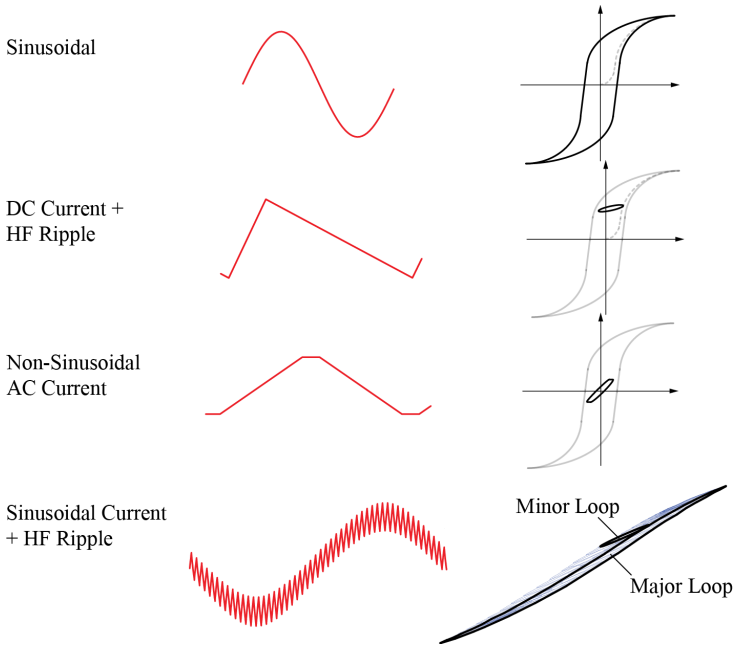

Source: Mühlethaler (2012).

resistance of the windings.

Dos Santos (2019) performed detailed studies on Electromagnetic Compatibility on Power Drive Systems for aircraft applications to optimize the system for the RTCA DO-160 standard constraints. The study consisted of system level and component level optimizations, where the system level focuses on high-frequency models and how they interact with system noise. The component level was focused on parasitics that affect noise coupling and has an influence on its attenuation.

Hoffmann Sathler (2021) also optimized a Power Drive System for aircraft applications with a focus on multi-objective design for losses and weight. The design of magnetic components on the input filter was simplified and did not take into account core losses and thermal modelling because thermal constraint is not very important in this case due to low core losses.

3.3 Chapter Conclusions

With the literature presented, we could see that there are several attempts of integrating the differential-mode inductor into the common-mode choke. However, solutions presented use unoptimized materials such as ferrite, that have low saturation flux density, which makes the resulting component to be bulky. However, some of these works present

interesting ideas on how to make a compact leakage layer for the CM choke.

This work will focus on component-level optimization, meaning that the dual-mode inductor will be designed to fit the given values of DM and CM inductance and system specifications. In that sense, no system-level optimization will be performed to find the best inductance values to meet specific standards; the focus is on the component itself. Thermal and core loss model will also not be needed since iron losses will be very low due to the application.

Chapter 4

Modeling of the Dual-Mode Inductor

In this chapter, a topology for the Dual-Mode inductor will be chosen and a reluctance circuit model for both differential and common modes will be developed. Afterwards, an air gap reluctance model will be developed to consider fringing effects of magnetic flux.

4.1 Topology choice

Many different ways of increasing leakage inductance of magnetic components were presented in Section 3.1, and, from Section 2.2, we have seen that the use of nanocrystalline cores is the most adequate for EMI filters due to high saturation flux density and good performance at high frequency. To choose the best topology for the Leakage Layer of the nanocrystalline tape-wound cores, a configuration in which the magnetic flux is always tangential to the layers formed by the ribbons is essential to reduce losses. This happens because, in tape wound cores, a magnetic flux tangential to the thin layers produces low eddy currents due to the small area of the ribbons cross section. Nevertheless, if this flux flows in the orthogonal direction, the area in which the flux crosses will increase, therefore increasing eddy currents and leading to higher losses (Cougo and Kolar, 2012). Fig. 4.1 exemplifies this phenomenon.

Like this, the Leakage Layers must be adapted to always have tangential flux in the tape-wound layers. Therefore, the most compact solution is to use two leakage layer blocks placed sideways to the tape-wound core as in Fig. 3.2(d). In this case, the leakage flux flows through both materials. However, the magnetizing flux flows through the tape wound core only and thus it is not necessary to cut through the layers of the nanocrystalline core to allocate the leakage path's block, which can produce interlamination short circuits and increase losses (Cougo et al., 2011).

The proposed integrated CM/DM inductor can be seen in Fig. 4.2. It consists of a nanocrystalline toroidal core and two iron powder blocks as the alternative magnetic paths for the DM flux. These objects are called Adapted Leakage Layers (ALL), as called

Figure 4.1: (a) Tangential flux produces low losses due to small Eddy currents. (b) Flux perpendicular to the layers produces high losses due to the increase in Eddy currents caused by the greater area. (c) Eddy current visualization of tangential and orthogonal flux on nanocrystalline core ribbons.

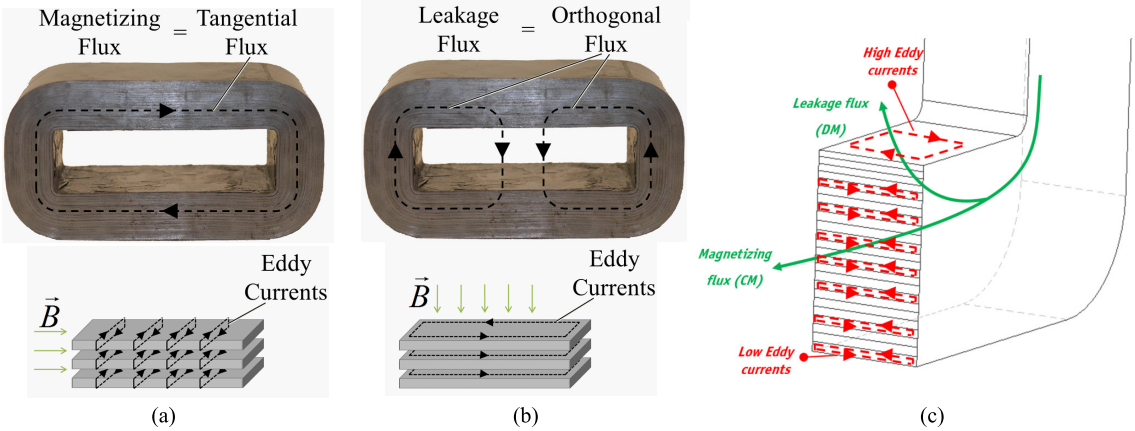

Source: Cougo and Kolar (2012).

by Cougo and Kolar (2012), and are separated from the toroidal core by air gaps. There are windings on the toroidal core, with N_m turns, and on the "ALL" blocks, there are N_b turns. As shown by Cao et al. (2022), the bobbins on the leakage layers allow increasing the leakage inductance without affecting the magnetizing inductance.

Figure 4.2: Model of the integrated DM/CM inductor and winding connections.

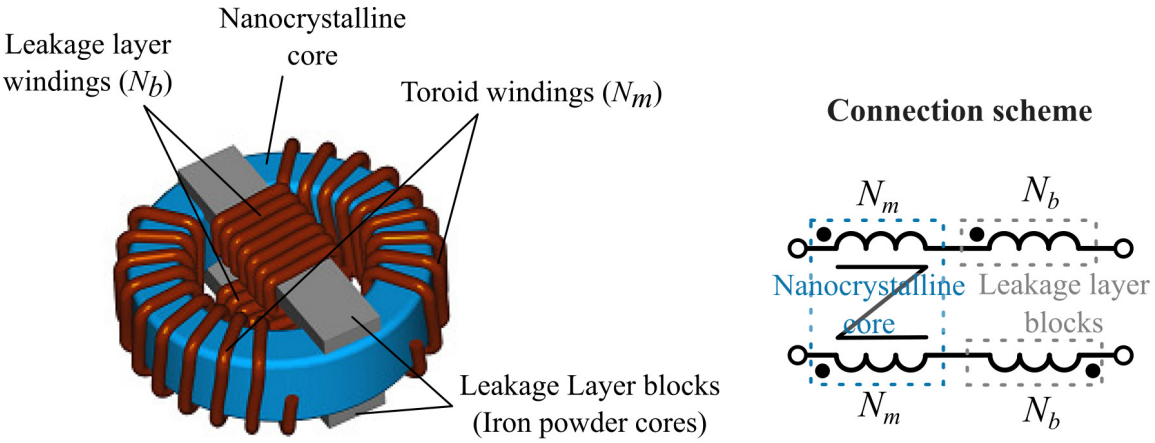

Source: Author.

4.2 Reluctance model of the Dual-Mode Inductor

A reluctance model of the proposed object will be presented to obtain the equationss for differential and common mode inductances.

4.2.1 Differential mode

The DM flux paths are illustrated in Fig. 4.3. The input currents I_{dm} of each CM choke winding (N_m) are opposite, resulting in the magnetic flux circulating in opposite directions within the core ($\Phi_{n,dm}$) and into the adapted leakage layer paths ($\Phi_{b,dm}$). Note that the leakage flux in the CM choke flows through the leakage layer and is increased by the leakage layer windings.

Figure 4.3: Magnetic field paths across the inductor for DM.

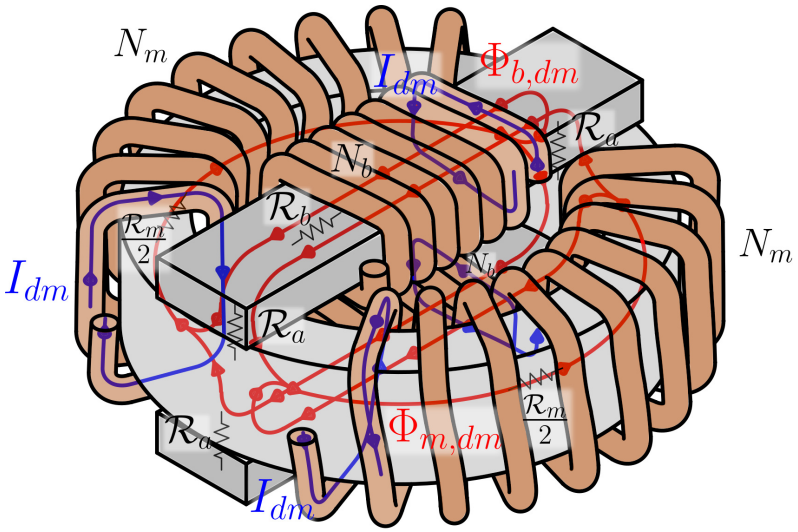

Source: Author.

The addition of leakage layer bobbins introduces two sources of magnetomotive force, and the inductor can be represented by the reluctance circuit model shown in Fig. 4.4. The reluctance calculation will be shown later in 4.2.3.

$\mathcal{R}_m$, $\mathcal{R}_w$, $\mathcal{R}_a$ and $\mathcal{R}_b$ represent the nanocrystalline toroid reluctance, the window leakage path reluctance, the air gap reluctance and the iron powder block reluctance, respectively. The calculation of these parameters will be presented in Section 4.2.3.

Using the superposition theorem and considering each half of the circuit symmetric, toroid and block DM magnetic fluxes ($\Phi_{m,dm}$ and $\Phi_{b,dm}$, respectively) can be obtained as

Figure 4.4: Integrated inductor reluctance equivalent circuit for differential mode.

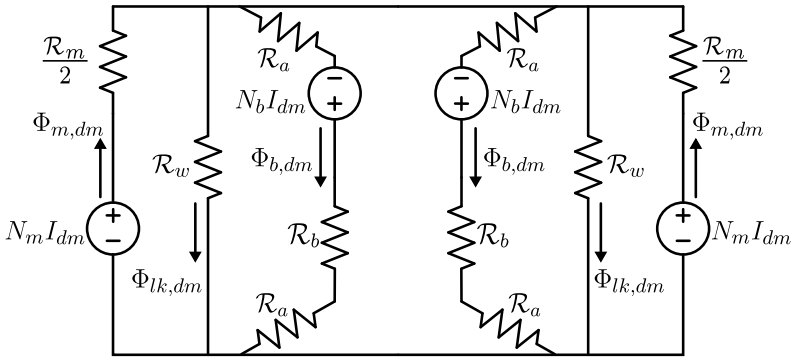

Source: Author.

follows.

$$\Phi_{m,dm} = \frac{N_m I_{dm}}{\frac{\mathcal{R}_m}{2} + (\mathcal{R}_w \parallel \mathcal{R}_x)} + \frac{N_b I_{dm}}{\frac{\mathcal{R}_m}{2}\left(1 + \frac{\mathcal{R}_x}{\mathcal{R}_w}\right) + \mathcal{R}_x} \tag{4.1}$$

$$\Phi_{b,dm} = \frac{N_b I_{dm}}{\mathcal{R}_x + \left(\mathcal{R}_w \parallel \frac{\mathcal{R}_m}{2}\right)} + \frac{N_m I_{dm}}{\frac{\mathcal{R}_m}{2}\left(1 + \frac{\mathcal{R}_x}{\mathcal{R}_w}\right) + \mathcal{R}_x} \tag{4.2}$$

Where $\mathcal{R}_x = 2\mathcal{R}_a + \mathcal{R}_b$. Therefore, the differential mode inductance can be obtained as

$$L_{dm} = \frac{\lambda_{dm}}{I_{dm}} = \frac{2(N_m \Phi_{m,dm} + N_b \Phi_{b,dm})}{I_{dm}} \tag{4.3}$$

$$L_{dm} = 2\left(\frac{N_m^2}{\frac{\mathcal{R}_m}{2} + (\mathcal{R}_w \parallel \mathcal{R}_x)} + \frac{2N_m N_b}{\frac{\mathcal{R}_m}{2}\left(1 + \frac{\mathcal{R}_x}{\mathcal{R}_w}\right) + \mathcal{R}_x} + \frac{N_b^2}{\mathcal{R}_x + \left(\mathcal{R}_w \parallel \frac{\mathcal{R}_m}{2}\right)}\right) \tag{4.4}$$

4.2.2 Common mode

For the common-mode, the flux paths are shown in Fig. 4.5 and the reluctance circuit is shown in Fig. 4.6.

Both the leakage layer windings and toroid windings produce flux linkage that contributes to the total common-mode inductance, as seen as follows.

$$\Phi_{m,cm} = \frac{N_m I_{cm}}{(\mathcal{R}_m/2)} \tag{4.5}$$

$$\Phi_{b,cm} = \frac{N_b I_{cm}}{2\mathcal{R}_a + \mathcal{R}_b} \tag{4.6}$$

The total CM inductance can be obtained by

Figure 4.5: Magnetic field paths across the inductor for CM.

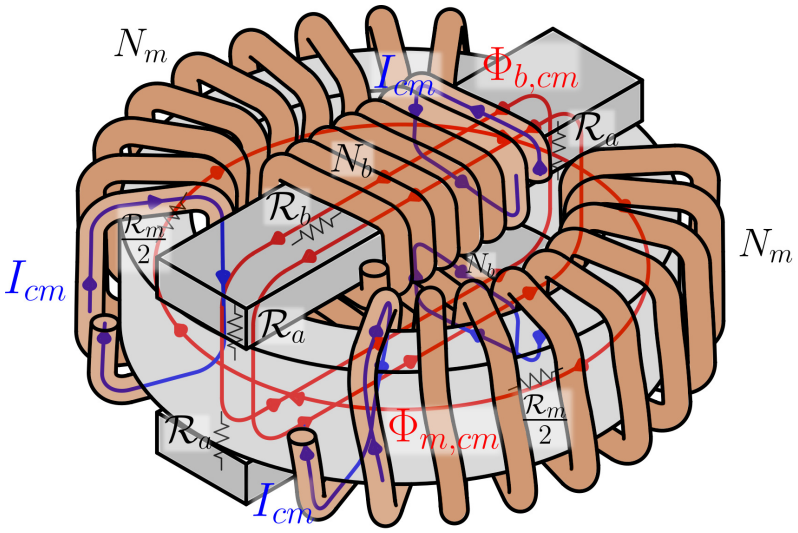

Source: Author.

Figure 4.6: Integrated inductor reluctance equivalent circuit for common-mode.

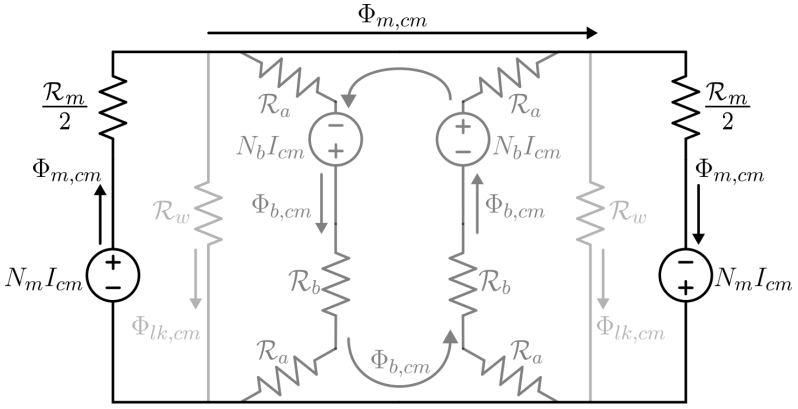

Source: Author.

$$L_{cm} = \frac{\lambda_{cm}}{I_{cm}} = \frac{N_b \Phi_{b,cm}}{I_{cm}} - \frac{N_b(-\Phi_{b,cm})}{I_{cm}} + \frac{N_m \Phi_{m,cm}}{I_{cm}} - \frac{N_m(-\Phi_{m,cm})}{I_{cm}} \tag{4.7}$$

This leads to

$$L_{cm} = \frac{4N_m^2}{\mathcal{R}_m} + \frac{2N_b^2}{2\mathcal{R}_a + \mathcal{R}_b} \approx 4N_m^2 A_L \tag{4.8}$$

Where A_L is the inductance factor of the core.

It should be noted that the first fraction of the equation contributes significantly to the overall inductance value due to the fact that the reluctance of the nanocrystalline core is several orders of magnitude lower than that of the leakage layer. This is a consequence of the high relative permeability of the toroidal core, which ranges from 1000 to 100000, and the low relative permeability of the leakage layer blocks and high reluctance of the air gaps.

4.2.3 Reluctance calculation

To obtain the reluctance values for each magnetic path, we can consider the dimensions for the toroidal core and for the Leakage Layer blocks as shown in Fig. 4.7.

Figure 4.7: Proposed CM Choke integrated with DM Choke. (a) 3D Perspective view. (b) 2D side view.

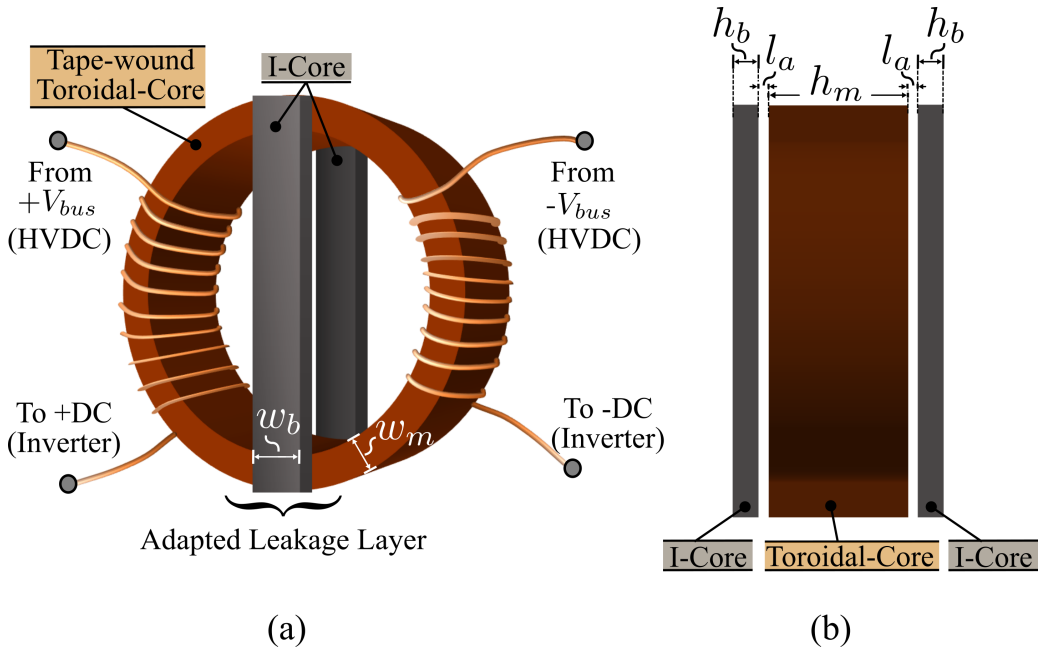

Source: Author.

The Leakage Layers both have three reluctances: two for the air gap between the toroid and the I-type block ($\mathcal{R}_a$), and one for the I-type block itself ($\mathcal{R}_b$). Additionally, $\mathcal{R}_m$ represents the reluctance of the toroid and $\mathcal{R}_w$ represents the window area leakage reluctance.

In that regard, reluctances of the magnetic objects can be approximated as

$$\mathcal{R}_b = \frac{l_b}{\mu_0 \mu_{rb} w_b h_b} \qquad \mathcal{R}_m = \frac{l_m}{\mu_0 \mu_{rm} A_e} = \frac{1}{2A_L} \tag{4.9}$$

where μ_0 is the Vacuum permeability, μ_{rb} is the adapted leakage layer (I-type block) relative permeability, and μ_{rm} is the permeability of the toroid material. Variables l_b and l_m represent the mean length of the I-type block and toroidal core, respectively. A_e corresponds to the effective cross-section area of the toroid and w_b is the block width. Variable A_L is the inductance factor of the toroidal core.

The approach developed by Balakrishnan et al. (1997) was used to account for the effects of fringing of the magnetic flux to calculate the reluctances of the air gap ($\mathcal{R}_a$) and window area ($\mathcal{R}_w$). The window area leakage reluctance can be written as

$$\mathcal{R}_w = \frac{l_b - 2w_m}{\mu_0 w_b (2l_a + h_m)} \tag{4.10}$$

The air gap reluctances can be obtained from Fig. 4.8, which shows the reluctance paths from a cross-sectional view of the object and from Fig. 4.9, which shows the decomposition of a side leg to calculate the air gap inductance using expressions in Balakrishnan et al. (1997).

Figure 4.8: Reluctance paths over a cross-sectional view of the inductor.

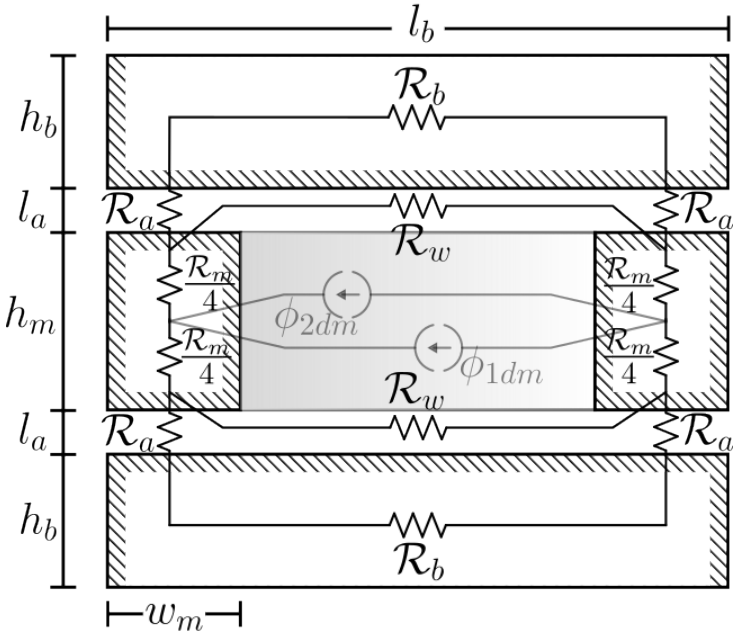

Source: Author.

Figure 4.9: Configuration of an air gap for reluctance calculation in the x-axis.

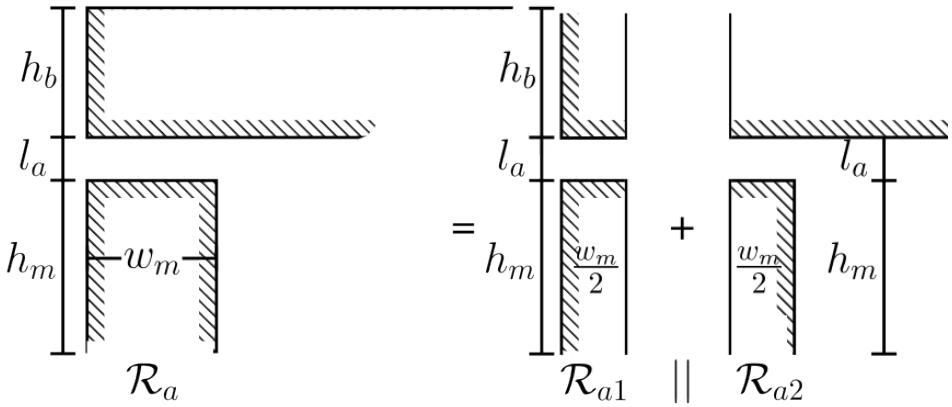

Source: Author.

In this context, the air gap reluctance can be approximated as follows.

$$\mathcal{R}_{a1}[\text{m/H}] = \frac{1}{\mu_0 \left(\frac{w_m}{2l_a} + \frac{2}{\pi} \left(1 + \ln \frac{\pi h_m}{4l_a} \right) \right)} \tag{4.11}$$

$$\mathcal{R}_{a2}[\text{m/H}] = \frac{1}{\mu_0 \left(\frac{w_m}{2l_a} + \frac{1}{\pi} \left(1 + \ln \frac{\pi \cdot \min(h_m, h_b)}{2l_a} \right) \right)} \tag{4.12}$$

$$\mathcal{R}_a = \frac{\mathcal{R}_{a1}\mathcal{R}_{a2}}{\mathcal{R}_{a1} + \mathcal{R}_{a2}} \cdot \frac{1}{w_b} \tag{4.13}$$

where w_b is the I-block width, as seen in Fig. 4.7(a), and l_a is the air gap length. Expressions in (4.11) and (4.12) consider the longitudinal distance much higher than the air gap distance. Therefore, the fringing effect in the y-axis could be ignored.

In the case studied, taking this assumption would lead to imprecisions because the leakage layer block's width is in a similar order of magnitude as the air gap length, which makes its fringing effect not negligible in both directions. Thus, it is possible to use the approach developed by Mühlethaler et al. (2011) to account for the three-dimensional effect of the air gap geometry.

For the x-axis, we can use (4.11) and (4.12) directly:

$$\mathcal{R}'_{ax}[\text{m/H}] = \frac{\mathcal{R}_{a1}\mathcal{R}_{a2}}{\mathcal{R}_{a1} + \mathcal{R}_{a2}} \tag{4.14}$$

For the y-axis, the geometry in Fig. 4.10 can be considered to obtain

$$\mathcal{R}'_{ay}[\text{m/H}] = \frac{1}{\mu_0 \left(\frac{w_b}{l_a} + \frac{4}{\pi} \left(1 + \ln \frac{\pi \cdot h_b}{4l_a} \right) \right)} \tag{4.15}$$

Figure 4.10: Configuration of an air gap for reluctance calculation in the y-axis.

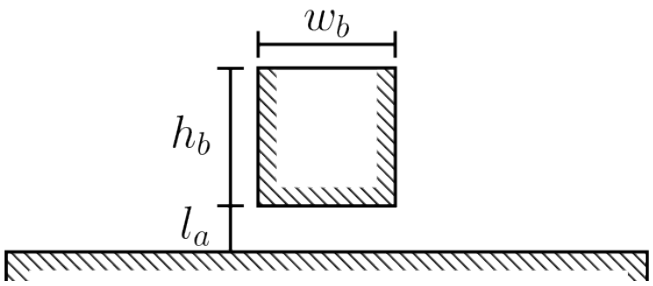

Source: Author.

We can define the fringing factor σ as the rate at which the reluctance calculated without considering fringing flux ($\mathcal{R}_a \approx \frac{l_a}{\mu_0 w_b w_m}$) changes with geometry in the x or y-axis. Therefore, the fringing factors can be defined as

$$\sigma_x = \frac{\mathcal{R}'_{ax}}{l_a/(\mu_0 w_m)} \qquad \sigma_y = \frac{\mathcal{R}'_{ay}}{l_a/(\mu_0 w_b)} \tag{4.16}$$

As a result, the total fringing factor can be obtained as

$$\sigma = \sigma_x \sigma_y \tag{4.17}$$

and the air gap reluctance can be calculated as

$$\mathcal{R}_a = \sigma \cdot \frac{l_a}{\mu_0 w_b w_m} \tag{4.18}$$

4.2.4 Total Flux

The total flux for each CMC winding flowing in approximately each half of the toroidal core can be seen as the superposition of the CM and DM parts, which results in

$$\Phi_T = \Phi_{m,dm} + \Phi_{m,cm} = N_m \left(\frac{I_{dm}}{\frac{\mathcal{R}_m}{2} + (\mathcal{R}_w \parallel \mathcal{R}_x)} + \frac{I_{cm}}{(\mathcal{R}_m/2)} \right) + \frac{N_b I_{dm}}{\frac{\mathcal{R}_m}{2}\left(1 + \frac{\mathcal{R}_x}{\mathcal{R}_w}\right) + \mathcal{R}_x} \tag{4.19}$$

4.3 Chapter Conclusions

In this chapter, a topology for the Dual-Mode inductor was chosen. It consists of a CM choke based on a toroidal nanocrystalline core with two adapted leakage layer blocks crossing the main window sideways to prevent orthogonal flux inside the nanocrystalline ribbons.

In sequence, reluctance circuit models were developed for differential mode and common mode behaviours. With these models the magnetic fluxes in each part could be calculated along with the DM and CM inductances. Furthermore, a detailed 3D air gap formulation was developed to account for effects of fringing flux on the DM inductance.

Chapter 5

Design Methodology and Optimization

In this chapter, the design optimization routine of the integrated inductor is presented. The main constraints and details of databases will be presented, as well as some analysis of sensibilities of different variables in the design. Finally, results from the optimization of a Dual-Mode inductor for a 50 kW Power Drive System input filter are shown and compared to an optimized discrete solution.

5.1 Optimization Routine

The procedure illustrated in Fig. 5.1 was used for the design optimization of the CM/DM inductor.

From system specifications, the values of common-mode and differential-mode currents (I_{cm} and I_{dm}) and inductances ($L_{cm,ideal}$ and $L_{dm,ideal}$) are defined. Databases of commercial nanocrystalline cores and iron powder materials are used to search for the best configuration of available geometry and materials.

Cores from manufacturers Vacuumschmelze (VAC) and Magnetec were used for the nanocrystalline database. Materials' relative permeabilities range from $\mu_m = 1000$ to 100000 and possible geometries are toroidal or oblong cores, with external diameters from 11 to 200 mm. This leads to a total of 157 core options.

The chosen materials for the iron powder database were the KoolMμ and XFlux from Magnetics Inc. These materials are the ones in which the I-Block cores are commercially available in relative permeabilities of 14, 26, 40 and 60. The XFlux has higher saturation flux density: 1.6 T versus 1.0 T from the KoolMμ. However, it has higher mass densities for similar permeability levels.

Following the loading of the magnetic core information, the algorithm initiates a loop that varies the nanocrystalline core, leakage layer block material and geometry, and

Figure 5.1: Dual-mode inductor optimization flowchart.

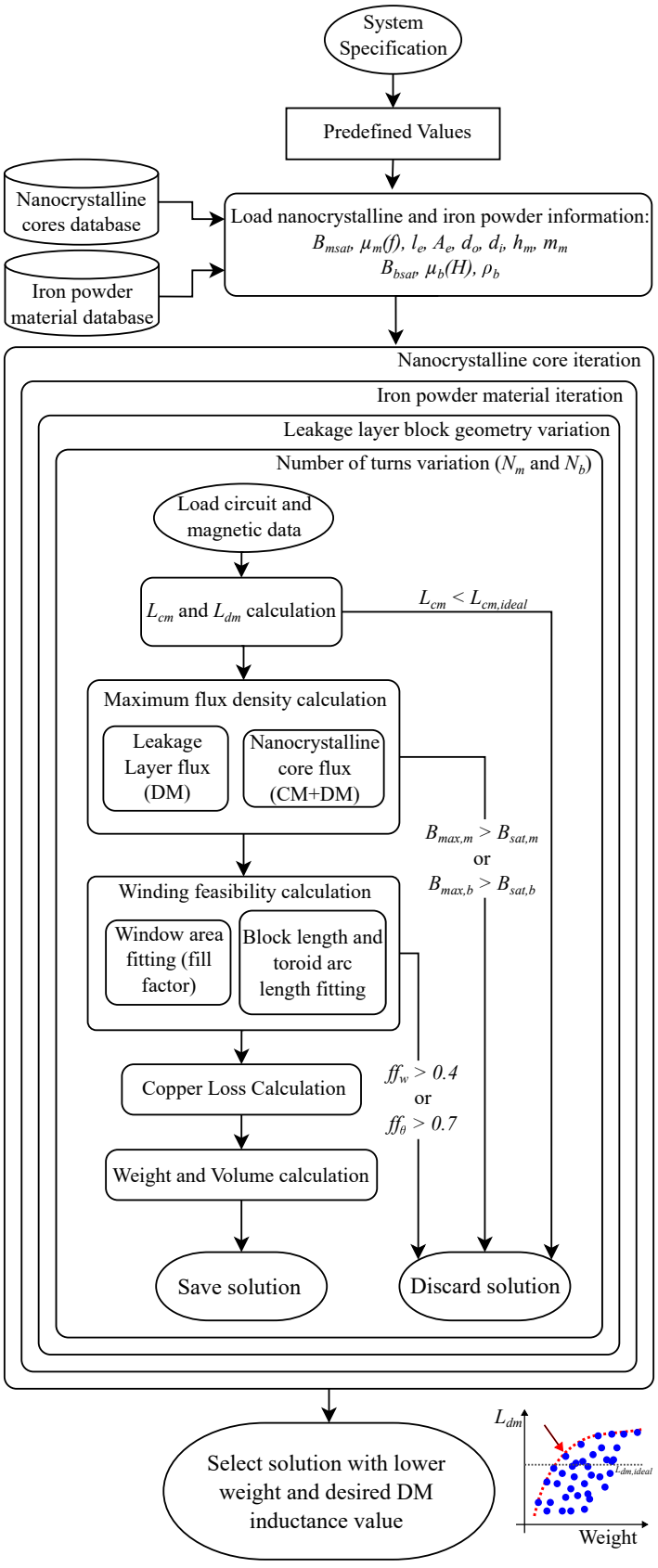

Source: Author.

the number of turns in block and toroid windings. As this is a brute-force search, the algorithm may require significant amount of time to complete. To reduce this time, one can conduct experiments to limit the variables' ranges and identify the most suitable search intervals for each variable.

Inside the loop, the inductor calculation function loads the circuit and magnetic data of the current iteration and calculates the DM and CM inductances according to (4.3) and (4.8). For L_{dm} calculation, the permeability roll-off due to DC magnetization is taken into account and to calculate L_{cm} the nanocrystalline core inductance factor at 100 kHz was used. If one of the calculated values is below the required inductance, the solution is discarded.

The air gap length was initially treated as a variable, but as illustrated in Fig. 5.2, optimal solutions for weight are consistently observed at lower air gap values. The graph shows the differential-mode inductance as a function of air gap length for various values of block height (h_b) for a specific dual-mode inductor solution. It is observed that the lower the air gap length, the higher the DM inductance, and, for equal DM inductance levels, the flux density is the same. Therefore, shorter air gap lengths are necessary to minimize the leakage layer weight, which is proportional to h_b.

Figure 5.2: Effects of leakage layer block height (h_b) and air gap length on DM inductance and block flux density. To minimize leakage layer weight, minimal air gap lengths are the most suitable, as the highest DM inductance values for each block height are consistently observed at low air gaps.

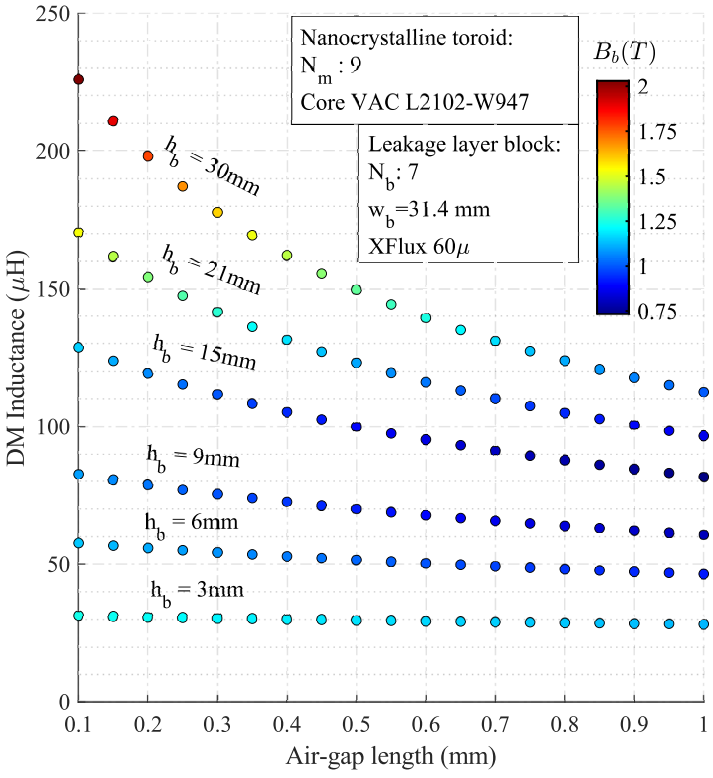

Source: Author.

It can thus be concluded that the most appropriate method for adjusting the DM inductance values is to maintain the air gap at a shorter length (0.1 mm in practice) and vary the parameters of the blocks, specifically their height, width and material. In order to achieve this air gap, it is necessary to cut the plastic case, which has a thickness of 700 to 1000 μm, and place a calibrated air gap sheet between the blocks and the toroid.

Following the execution flow, the next step is to calculate the maximum flux density inside both the nanocrystalline core and leakage layer block. To keep the solution, the values must be below the saturation flux density of the corresponding materials of the current iteration.

Subsequently, the feasibility of winding is evaluated. The wire diameter and number of strands may be predefined values or may be calculated for a maximum current density value. Once the aforementioned parameters have been defined, it is necessary to ensure that the toroid windings are able to fit along the available inner angular length of the toroid in a single layer. This is done to reduce the parasitic capacitances in common mode. Furthermore, the block windings must be wound in a single layer, with the available space being the inner diameter of the toroid. Consequently, a maximum occupation of 70% has been defined for these lengths. Additionally, a window area filling factor of 40% has been defined for the winding process to be feasible.

Fig. 5.3 shows how the maximum differential-mode inductance varies with the nanocrystalline core permeability μ_m. For high relative permeability values, the maximum number of turns that saturate the core is the limiting factor, while on low permeability, the winding feasibility limits the DM inductance. The graph shows that there is an optimal value of the toroidal core material relative permeability for each leakage layer winding configuration.

On the right side of the graph, the multiple steps are due to the discrete number of N_m windings and the saturation flux density is what limits the maximum DM inductance value. Higher values of μ_m lead to a reduced number of turns because the core saturates more easily, which results in low DM inductance values. On the left side, the maximum feasible number of turns is achieved because the core does not saturate and the DM inductance reduces for lower μ_m values due to the reluctance increase. Therefore, the maximum DM inductance value occurs at the highest relative permeability value where the maximum number of turns is reached.

The graph also shows that the best optimized nanocrystalline materials for the dual-mode inductors are the "low permeability" types (μ_m ranging from 3000 to 4000). These materials, while maintaining the good performance of high permeability nanocrystalline at high frequency, allow a higher number of turns without increasing the common-mode inductance too much. In this way, the differential-mode inductance benefits from the high number of turns on the toroid and can reach higher values without saturating the core due to the common-mode inductance.

Figure 5.3: Maximum DM inductance for different values of nanocrystalline core permeability μ_m and number of turns N_b on the block core.

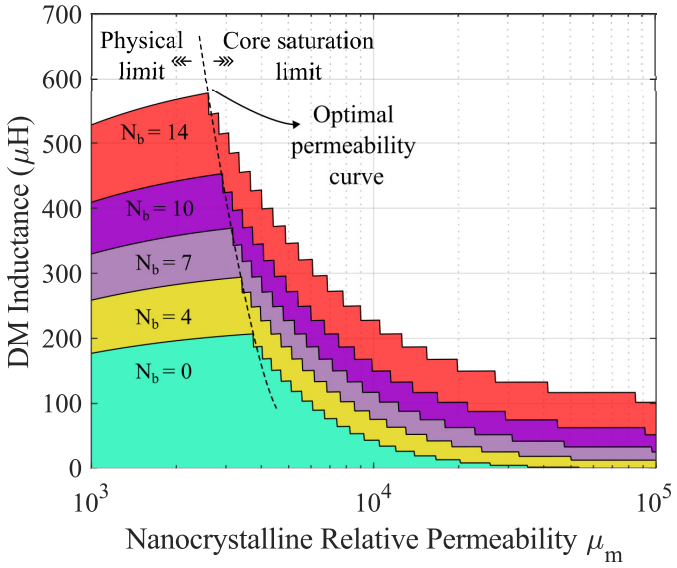

Source: Author.

5.2 Case study: 50 kW power drive input filter

To validate the optimization, an integrated inductor was designed for a 50 kW power drive and compared to an existing optimized filter using discrete inductors (DM inductor and CM choke). This filter can be seen in Fig. 5.4 and its data can be seen in Table 5.1.

Figure 5.4: Discrete input filter for 50 kW power drive (Hoffmann Sathler, 2021).

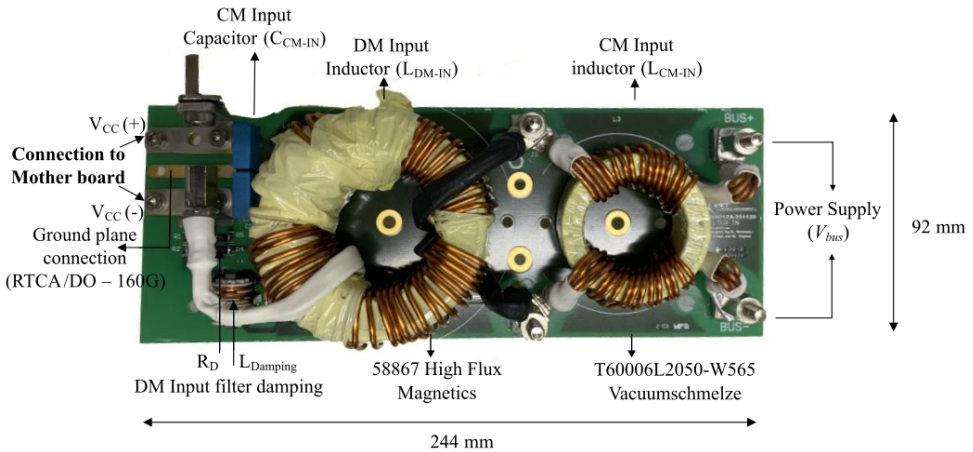

Source: Hoffmann Sathler (2021).

Design constraints and system specifications for both the dual-mode inductor and the discrete filter can be seen in Table 5.2.

Table 5.1: Discrete filter specification

Component	Inductance	Windings
DM inductor	$L_{dm} = 35.4\ \mu$H (at 92.6 A)	$N = 15$ per phase 4×12AWG
CM Choke	L_{cm}(10 kHz)$= 300\ \mu$H L_{cm}(100 kHz)$= 175\ \mu$H	$N = 4$ per phase 4×12AWG

Table 5.2: Design constraints for the inductors

Parameter	Value
Power (P)	50 kW
DC bus voltage (V_{dc})	540 V
DM current (I_{dm})	92.6 A
CM current (I_{cm})	1.0 A
Maximum current density (J_{max})	7.0 A/mm^2

Once these parameters were defined, the optimization routine was executed, resulting in the blue-dashed Pareto front depicted in Fig. 5.5. However, it should be noted that not all toroids and iron powder blocks were available for sale on the market. Consequently, another Pareto front was generated, this time using only the available cores, shown in red-dashed. In this context, the selected solution represents an optimal option with restritions that nevertheless outperforms the traditional topology, but is around 10% heavier than the optimal solution. Table 5.3 shows the specifications of the selected Dual-mode inductor.

Table 5.3: Dual-mode inductor results

Parameter	Value
Nanocrystalline core ***Relative Permeability*** μ_m	Magnetec M-683 4000
Leakage layer material ***Block dimensions (mm)***	KoolMu 26μ $17.6 \times 11 \times 80$
Number of turns N_m ***Number of turns*** N_b	9 (4×12AWG) 6 (4×12AWG)
CM inductance L_{cm} ***DM inductance*** L_{dm}	347.5 μH 37.7 μH

When analyzing the maximum achievable DM inductance curve for the inductor geometry found in Fig. 5.6, we can see that the chosen design is very close to the optimal nanocrystalline permeability curve. This shows that the designed inductor is close to ideal for the available core geometries and permeabilities.

Graph in Fig. 5.7 shows relative comparisons between the Dual-mode inductor and the discrete solution in terms of losses, weight, area and volume. Reductions of 20.5% in weight and 14% in losses were observed. To calculate the area used by the objects, the connections and the inductor-circumscribed square areas were taken into account. In this

Figure 5.5: Pareto front optimization result for the CM/DM inductor for 50 kW motor drive input filter application.

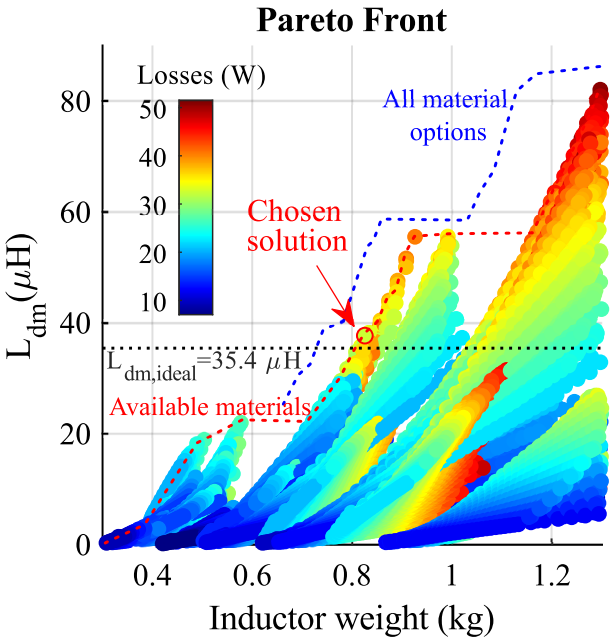

Source: Author.

Figure 5.6: Maximum achievable DM inductances for the selected core geometries and materials for diferent values of N_m and N_b.

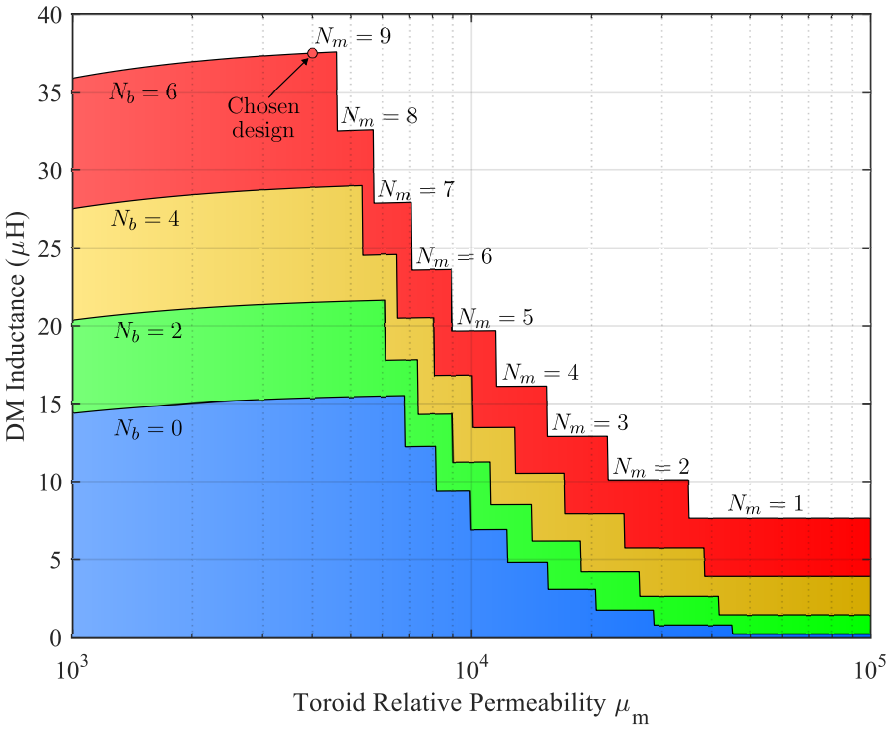

Source: Author.

regard, the area occupied was reduced by 33.8%, because the M-683 nanocrystalline core is approximately the same size as the High Flux 58867 core, and the number of connections

is reduced. However, the volume occupied by the integrated inductor is 16.2% higher than the discrete solution due to the additional height of the leakage layer blocks and windings.

Figure 5.7: Comparison graph between the optimal Dual-mode inductor and the discrete solution for 50 kW power drive input filter.

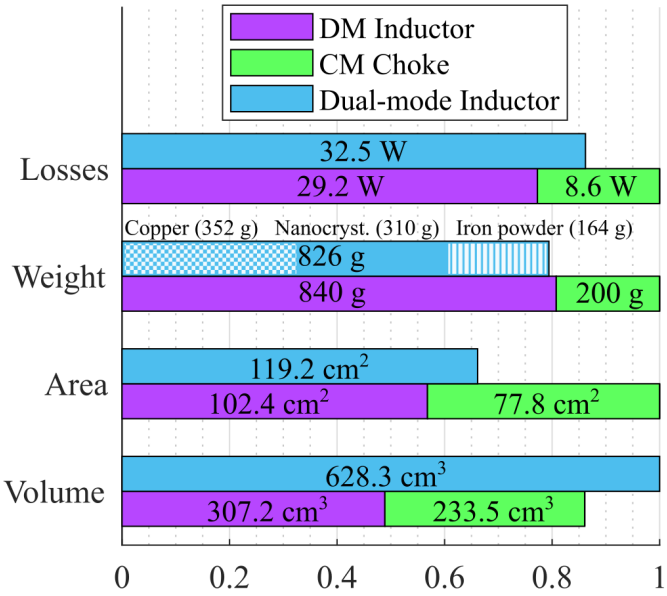

Source: Author.

5.3 Chapter Conclusions

This chapter presented a multi-objective optimization algorithm that used the analytical model developed in Chapter 4 to maximize the DM inductance and minimize the magnetic component weight and losses. A case study was developed and consists of optimally designing a dual-mode inductor for a 50 kW power drive input filter and comparing it to an existing optimized traditional discrete inductors solution. Results show a potential reduction of 20% in weight, 14% in losses and 34% in PCB area.

Chapter 6

Results

In this chapter, the validation of the developed reluctance models will be presented and both 2-dimensional and 3-dimensional air gap reluctance formulations will be compared to Finite Element Analysis (FEA) simulations and experimental results. In the sequence, a prototype of the integrated inductor developed in Section 5.2 is produced and tested to validate the optimization results and compare it to the traditional filter solution.

6.1 Model Validation

To assess the integrated CM/DM reluctance inductor reluctance model, several simulation and experimental tests were performed. The object used to validate the model consists of a CM inductor with $N_m = 14$ turns on each side and a Vitroperm 500F Nanocrystallin toroidal core, PN T600006-L2090-W518 from VacuumSchmelze. The leakage layers were made with two ferrite I-core blocks from Ferroxcube (PN I93/28/30-3C94) with no windings ($N_b = 0$), as the objective is to validate the reluctance model. Additionally, a set of 0.25 mm air gap sheets was used to vary the air gap length during the experimental tests. The inductor under test can be seen in figure 6.1. The ferrite block is used because of disponibility and due to the fact that its reluctance is negligible in comparison to the air gap reluctances. Therefore, it is adequate to use ferrite instead of iron powder to evaluate the air gap reluctance model.

6.1.1 Small Signal Tests

The first set of tests consists on measuring the CM and DM inductance of the inductor with an impedance analyzer (Keysight E4990A). Figure 6.2 exemplifies how

Figure 6.1: Prototype Overview. (a) Perspective view. (b) Top view.

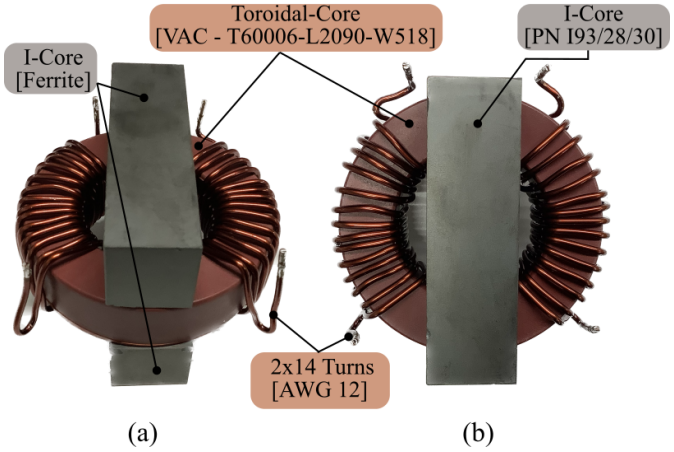

Source: Author.

these measurements were done. It should be noted that connections for CM are made in series, which increases the inductance by four times due to the doubled number of windings.

The graph of figure 6.3 shows DM and CM inductances as a function of frequency for the inductor with and without the leakage layer blocks. Measurements at 10 kHz indicate DM inductance $L_{dm} = 106.2\,\mu H$ with the Adapted Leakage Layer and 30.7 µH for the conventional CM choke. Note that the CM inductance does not change its value with the addition of the leakage layer, but the DM inductance has its value multiplied by 3.5 times at 10 kHz. This value could be even higher if the minimum air gap length were not limited to the case thickness of 2.35 mm.

Figure 6.2: Experimental setup. (a) DM inductance (L_{dm}) and (b) CM inductance (L_{cm}).

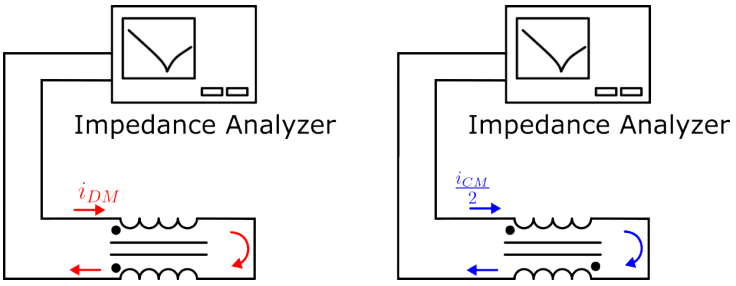

Source: Author.

6.1.2 Impact of air gap length on DM inductance

To validate the model in different conditions, the DM inductance was evaluated for various values of air gap lengths. The minimum value is the toroidal core case thickness,

Figure 6.3: Experimental results. DM and CM inductances for the common-mode choke with (dashed lines) and without (solid lines) the ALL.

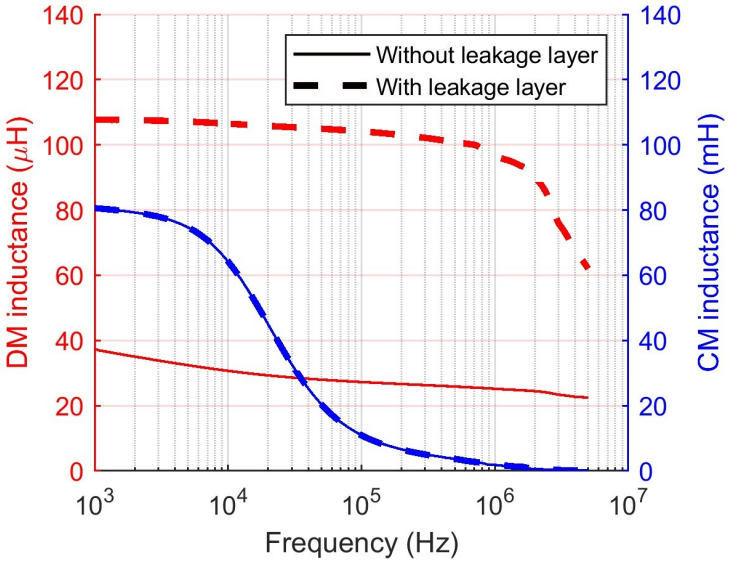

Source: Author.

which is 2.35 mm, and it was increased with the calibrated air gap sheets from 2.35 to 3.35 mm using one 250 μm-thick sheet at a time. Measurements used the same methodology as in the previous section. The same length variation was performed in 2D and 3D Finite Element Method (FEM) simulations, using FEMM and CST softwares respectively, and extended to lower and higher lengths.

Drawing representative 3D models of the object to be evaluated can be very time consuming. With that in mind, a Python script was developed to automate this design step and open the possibility to evaluate all desired solutions in FEM software. With that script, all that is needed is a string generated by the Matlab inductor model function used in the optimization routine with all necessary mechanical and winding data of the integrated inductor. More detail of this process can be seen in Appendix A.

Figures 6.4 and 6.5 exemplify the simulation models used for the parameter sweep of the air gap lengths.

The graph of Fig. 6.6 compares the low-frequency DM inductance (10 kHz) results. Lines show calculated values for the 2D model (4.13) and 3D analytical model (4.18) and the points show the results for the FEM simulations alongside the measured values. The 3D analytical model presents a maximum error of 6.1% in the measured interval, while the 3D FEM has a 1.3% maximum error when compared to measured values. The 2D model and FEM presented a much higher error of around 27.4%, which shows that the three-dimensional effects are not negligible and need to be considered for a more accurate model.

The graph illustrates that as the air gap length decreases, the 2D and 3D analytical models become more similar. This is due to the reduction in fringing effects as the field

Figure 6.4: Example of 2D Simulation result illustrating the impact and effects of fringing flux at air gap zone, using FEMM software.

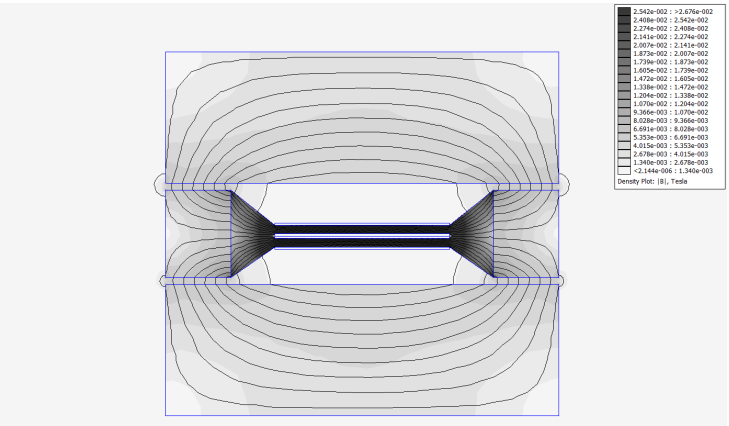

Source: Author.

Figure 6.5: Example of 3D FEM simulation of the CM/DM choke using CST software.

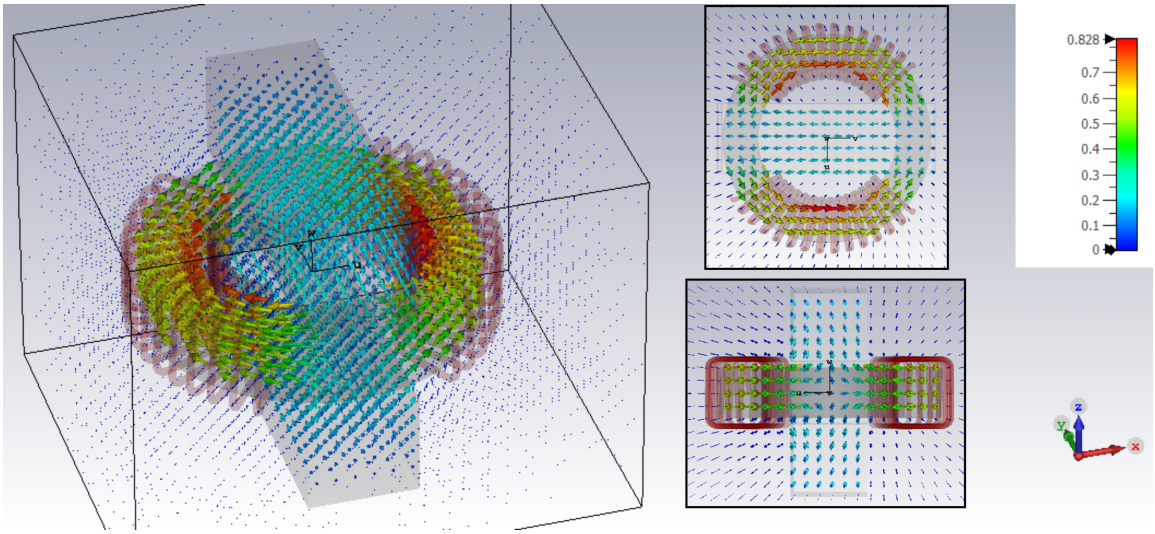

Source: Author.

lines become less spread. Results obtained using FEM simulations also follow this trend.

6.1.3 High-Power Test and Influence of Saturation

An alternative experiment can be considered to verify the influence of saturation of each magnetic core. It consists basically of driving a half-bridge converter with a single pulse to excite the inductor. The pulse width is fixed at a certain value and the DC bus voltage is increased gradually until the core saturates. Fig. 6.7 shows the experimental setup. Note that the connections for CM are made in series, which increases the inductance

Figure 6.6: Comparison between 2D and 3D models, FEM simulations and experimental results for DM inductance. The graph shows that the 3D model approximates well to the 3D FEM and experimental results.

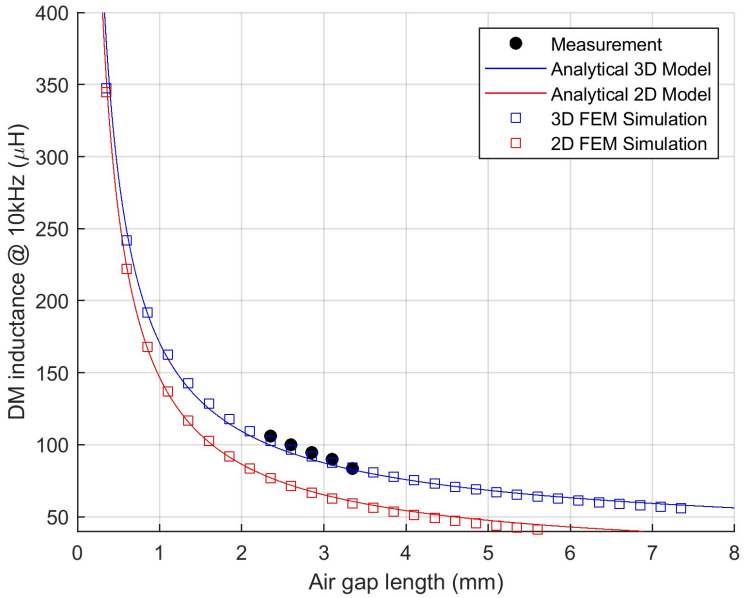

Source: Author.

by four times due to the doubled number of windings.

Figure 6.7: Experimental setup for the pulse test. (a) Overview. (b) DM Schematic. (c) CM Schematic.

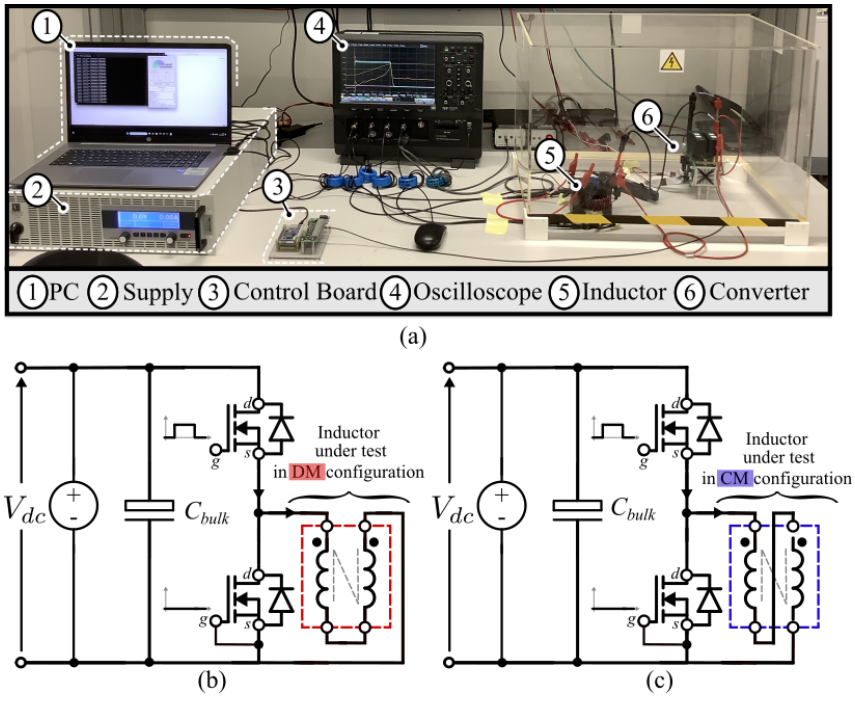

Source: Author.

A pulse of 110 V and 80 µs was applied in configuration of Fig. 6.7(b) to achieve saturation and observe the effects of high current in differential mode. As shown in

Fig. 6.8, the component saturates at the current of 77.6 A and the flux density (B) values in the moment of saturation for the nanocrystalline toroid and ferrite block are 1.18 T and 0.27 T, respectively.

Figure 6.8: Effects of saturation in DM for a pulse of 110 V, 80 µs.

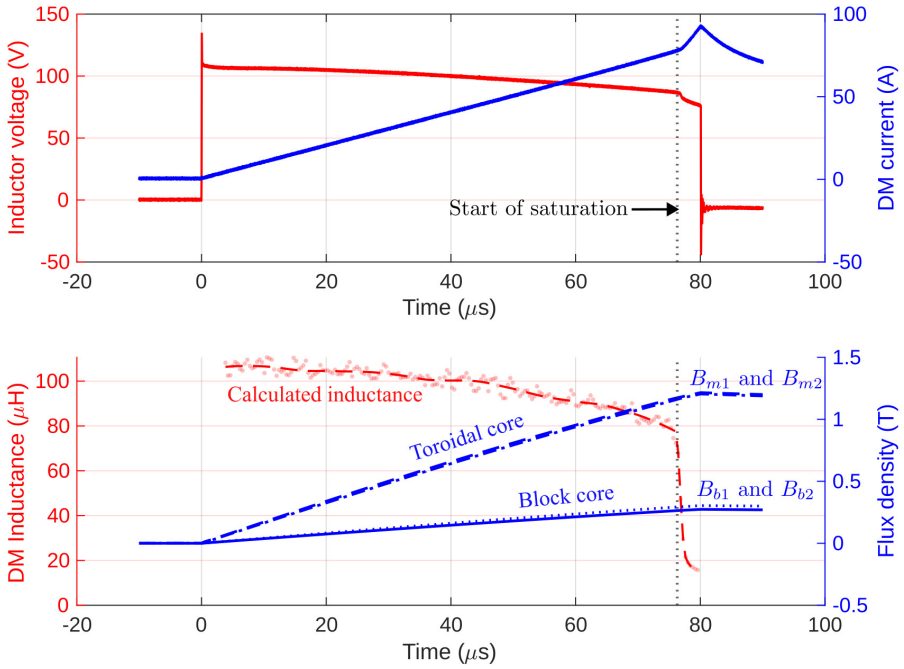

Source: Author.

The saturation of the component can be caused by either the ferrite block or the nanocrystalline toroid. To calculate the saturation currents of each material, the following equations can be derived from (4.19) when N_b is zero

$$I_{dm,sat,m} = \frac{B_{sat,m}A_{e,m}(2N_m) - L_{cm}I_{cm,sat}}{L_{dm}} \tag{6.1}$$

$$I_{dm,sat,b} = \frac{B_{sat,b}A_{e,b}(2N_m)}{L_{dm}} \tag{6.2}$$

$$I_{cm,sat,max} = I_{cm,sat,m}(I_{dm} = 0) = \frac{B_{sat,m}A_{e,m}(2N_m)}{L_{cm}} \tag{6.3}$$

The saturation flux density, B_{sat}, is extracted from the datasheet of each magnetic material. For the Vitroperm 500F, its value is 1.2 T and for the Ferroxcube ferrite, it is 0.38 T at 25°C. Table 6.1 compares the calculated and the measured currents and shows that the nanocrystalline core saturates first and that the analytical model corresponds well to the experimental value.

For common-mode, the configuration of Fig. 6.7 (c) is set up and a pulse of 170V and 40 µs is applied. Figure 6.9 shows the results of this test. The flux density in both leakage layer blocks is zero all the time and the nanocrystalline toroid saturates next to 1.15 T, with a CM current of 120.4 mA, very next to the value of 120.1 mA calculated from (6.3).

Table 6.1: Measurement results for saturation current.

	Calculated with analytical model	Measurement
$I_{sat,m}$	76.83 A	77.6 A
$I_{sat,b}$	89.63 A	

Figure 6.9: Effects of saturation in CM for a pulse of 170 V, 40 μs.

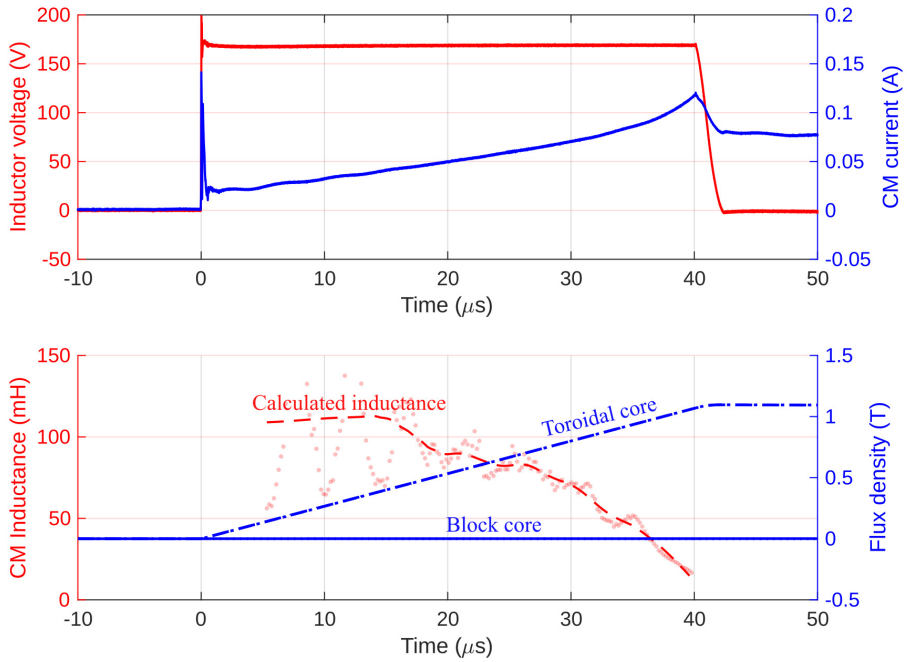

Source: Author.

6.1.4 Flux Distribution in Differential-Mode

Using the same experimental setup as the saturation test, the air gap sheets were positioned under only one of the leakage layer blocks and the magnetic flux was measured with bobbins of seven turns wound around each block and alongside the toroid windings. This way, the reluctance of one leakage path is constant and the other varies with air gap length. Therefore, the flux distribution in each leakage layer can be analyzed for unbalanced conditions and compared to the model predictions. Finally, the top block was completely removed, allowing the flux to pass only through the bottom block and the air.

Tables 6.2 and 6.3 show the magnetic flux and flux density values measured and calculated for 200 V and 20 μs pulses. Note that the value measured for the bottom leg differs from the calculated for about 13.2% when the air gap is minimum for both legs. This means that the case thickness of the superior and inferior faces of the toroid are not equal, which causes a deviation from the calculated values.

Another factor that impacts the precision of the analytical model is the modeling

of the flux leakage through the air, ϕ_{lk}. The developed model only considers a reluctance path in the window and does not include the winding or the outside path leakage. In that sense, the flux error in the ALL increases for higher air gap lengths, up to 32% when the top leakage layer is removed, and the flux leakage through the air has a constant 50% error in all cases.

Table 6.2: Magnetic flux along the CM/DM Choke parts.

$l_{a,2}$ (mm)		2.35	2.60	2.85	3.10	3.35	∞
ϕ_{b1} (μWb)	Calc.	134	138	141	144	147	242
	Meas.	116	120	124	127	131	183
ϕ_{b2} (μWb)	Calc.	134	130	126	122	119	0
	Meas.	130	123	119	114	109	0
ϕ_{m1} (μWb)	Calc.	143	143	143	143	143	143
	Meas.	140	140	140	140	140	136
ϕ_{m2} (μWb)	Calc.	143	143	143	143	143	143
	Meas.	144	143	143	142	142	139
ϕ_{lk} (μWb)	Calc.	18	19	19	20	20	44
	Meas.	37	39	40	40	42	91

Table 6.3: Flux density along the CM/DM Choke parts.

$l_{a,2}$ (mm)		2.35	2.60	2.85	3.10	3.35	∞
B_{b1} (mT)	Calc.	159	164	168	171	174	288
	Meas.	138	143	147	151	156	218
B_{b2} (mT)	Calc.	159	154	150	145	142	0
	Meas.	155	147	141	136	129	0
B_{m1} (mT)	Calc.	627	627	627	627	627	627
	Meas.	614	614	614	612	612	596
B_{m2} (mT)	Calc.	627	627	627	627	627	627
	Meas.	631	626	625	623	622	611

These errors in the flux densities in the ALL blocks may result in oversizing the leakage layer. To avoid it, it is necessary to have reliable and equal values for casing or coating thickness on each side of the toroidal core.

6.2 Prototype Fabrication

A prototype for the Dual-mode inductor was developed for the suboptimal design presented in Chapter 5 with the parameters in Table 5.3 in order to verify the integrated inductor's performance, to validate models and optimization routine and also to compare

it to the discrete chokes of Fig. 5.4. The obtained results were also compared to 3D Finite Element Method (FEM) simulations in CST software. The prototype is shown in Fig. 6.10.

Figure 6.10: Prototype of the Dual-mode inductor for a 50kW power drive input filter. (a) Top view and size comparison with the discrete filter. (b) Side view. (c) Front view.

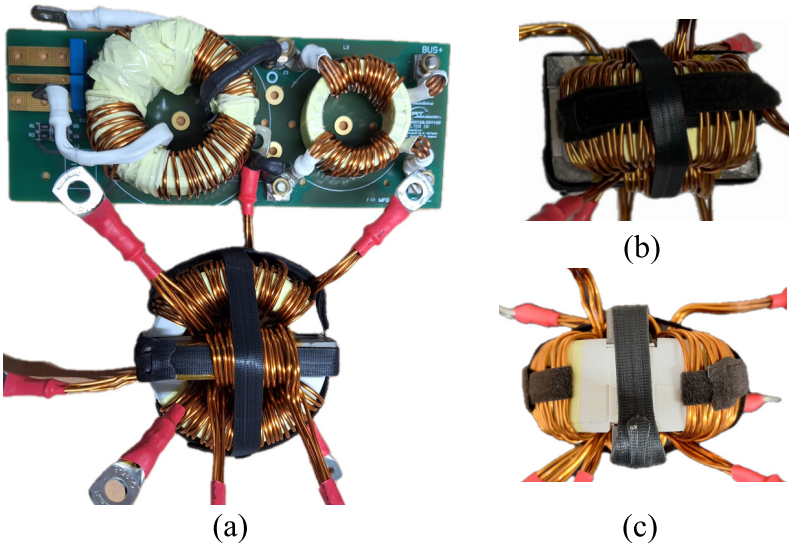

Source: Author.

The primary challenge during the fabrication process is the cutting of the nanocrystalline core casing and the precision machining of iron powder blocks to the desired geometries. In order to reduce the air gap length between the leakage layer blocks and the nanocrystalline core, it is necessary to either cut the plastic case at the contact area or fabricate a new case with the openings. The best solution found was to 3D-print a new case with the holes in the desired positions, as shown in Fig. 6.11. With regard to the leakage layer blocks, the desired geometries are not commercially available. Consequently, a larger I-block core was cut into smaller parts, requiring the use of appropriate equipment.

Figure 6.11: Fabricated case with Adapted Leakage Layer openings.

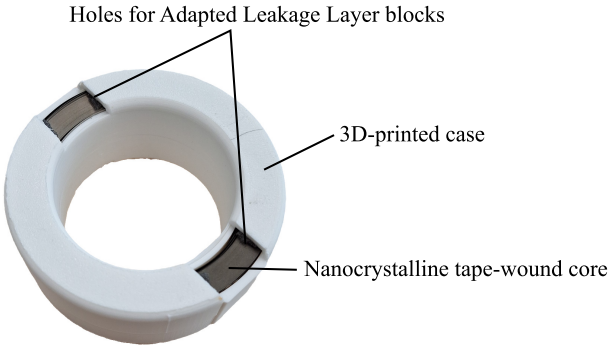

Source: Author.

In this context, the measured parameters of the fabricated prototype can be seen in Table 6.4.

Table 6.4: Prototype parameter values

Parameter	Meas. value	Model value	Cause of the difference
Total weight	1.03 kg	0.83 kg	204g of connectors and extra wire and block volume
Total DC resistance	4.8 mΩ	3.8 mΩ	Extra wire lengths and connection resistance

As seen in the table, the measured values differed from the predicted by the model because of the added weight of connectors, extra wire lengths and machining imprecisions of the iron powder blocks that led to volume increase. When summing the weight of extra wire lengths of 7 cm for each connection and a total of eight connectors, the added weight is 160 g. Each block was cut with an extra length of 5 mm and a section 19% higher, adding an extra 22 grams per block. Therefore, the added weight was about 204 g, which justifies the difference from the model. The excess DC resistance can be justified by the extra perimeter of the block due to the fabricated 3D-printed case, increasing the winding length, summed up with the extra wire lengths and the connection resistances.

6.3 Experimental Verification

To validate the optimization results, DM and CM inductances will be measured in frequency domain with an impedance analyzer. A high current pulse test will evaluate DM inductance roll-off and common-mode saturation current levels of both discrete and integrated solutions.

6.3.1 Small Signal Test

The first set of tests used an impedance analyzer Keysight E4990A to measure the CM and DM inductances of both integrated and discrete solutions in relation to the frequency. Graph of Fig. 6.12 shows measurements for common-mode and Fig. 6.13 for differential-mode inductances.

Figure 6.12: CM inductance measurement of the discrete and integrated solutions.

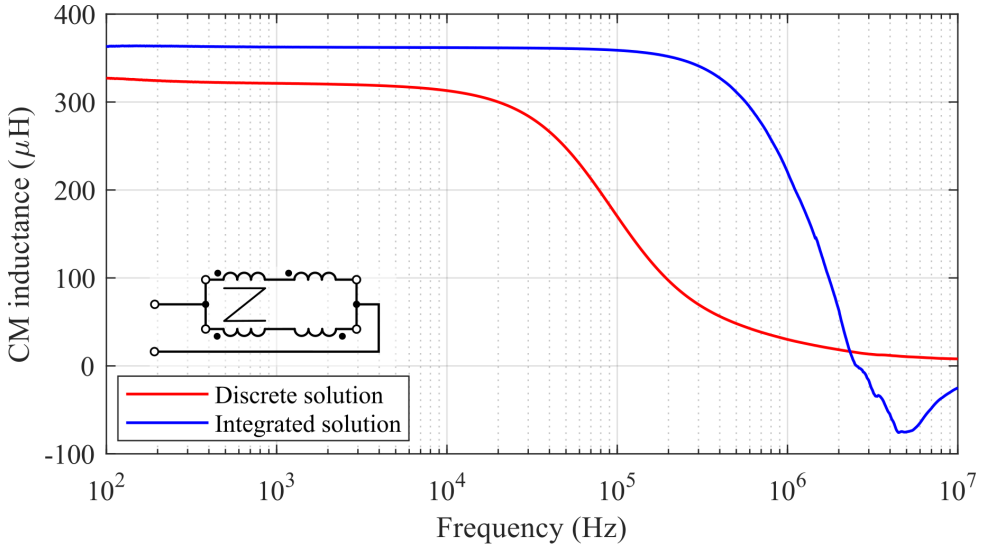

Source: Author.

Figure 6.13: DM inductance measurement of the discrete and integrated solutions.

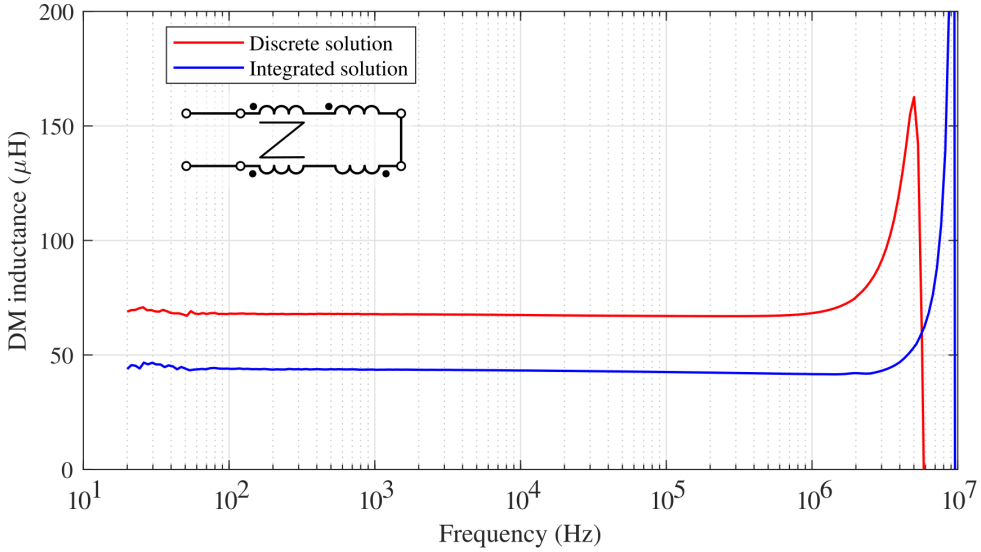

Source: Author.

Results for common-mode indicate that the CM inductance of the dual-mode inductor prototype was higher than that of the discrete CM choke (362.5 µH for the Dual-Mode and 307.5 µH for the CM choke at 10 kHz) and achieved a higher frequency coverage of about one decade. This is because the Dual-Mode inductor uses a low permeability nanocrystalline core ($\mu_r = 4000$), and the CM choke is composed of a higher permeability one ($\mu_r = 30000$). Therefore, for the same frequency, the low-permeability core will have a lower flux skin depth, which leads to lower eddy currents that produce opposing flux inside the core. However, this advantage comes with a tradeoff of a parasitic capacitance increase due to to the higher number of turns. This effect can be evaluated with an impedance measurement, as shown in Fig. 6.14.

Figure 6.14: CM impedance measurement of discrete and integrated solutions.

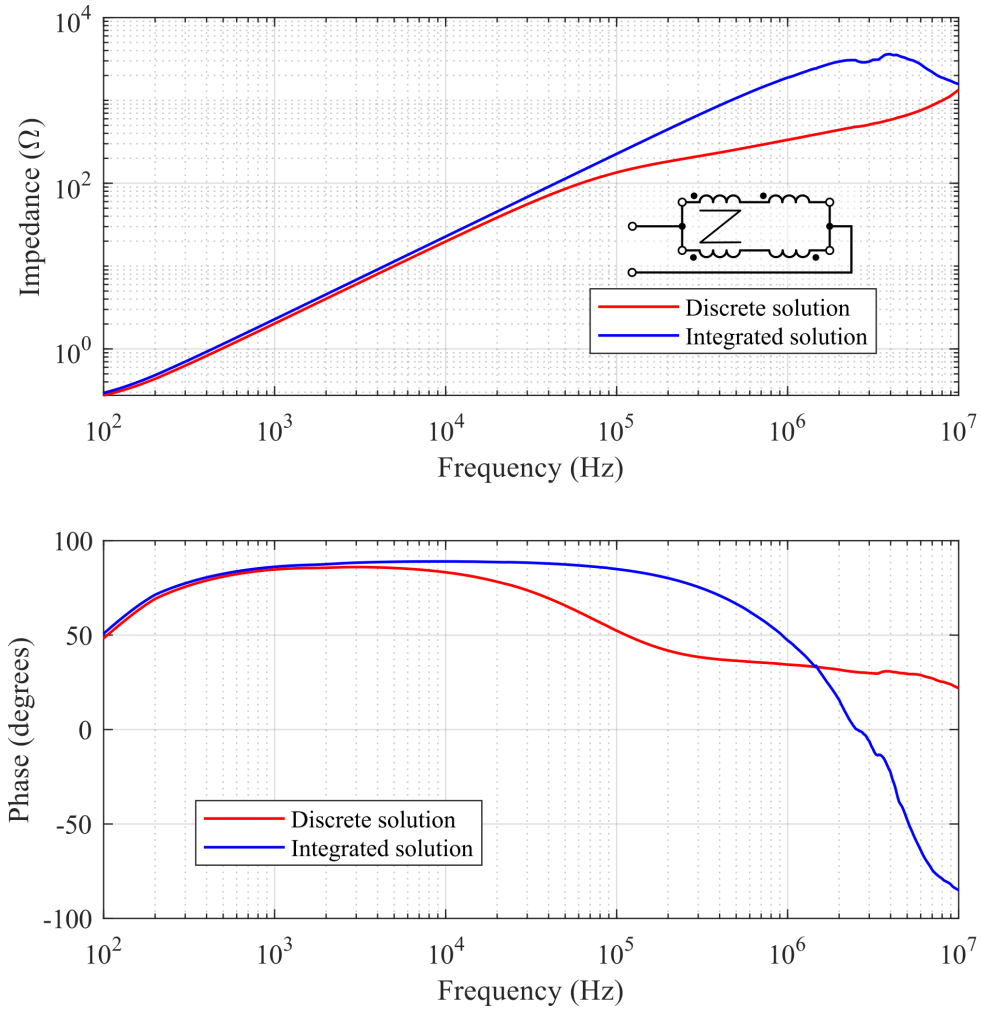

Source: Author.

The impedance curve of Fig. 6.14 shows that the CM impedance of the integrated inductor remains higher than that of the discrete solution until 10 MHz, where happens the impedance decay from the ressonance between the CM inductance and the parasitic capacitance. The higher stray capacitance of the integrated solution is due to a higher number of windings because of the use of "low permeability" nanocrystalline cores. However, in the design of Dual-Mode inductors, these types of cores are often the best choice since the windings on the toroidal core serve for both common-mode and differential-mode inductances, making it advantageous to maximize the number of turns on the nanocrystalline core. In that sense, the "low permeability" is necessary to avoid core saturation and its stray capacitance tradeoff can be manageble by maintaining design contraints such as single winding layer and minimal winding spacing.

For differential-mode, the initial inductance of the Dual-Mode inductor is lower than that of the discrete DM inductor (43 and 68 µH, respectively). But, since iron powder parts are used, the inductance roll-off at high current must be evaluated. Therefore, a high current pulse test was performed in both solutions to measure the DM inductance

at the nominal operation point.

6.3.2 High Power Test

The experimental setup for the high current pulse test can be seen in Fig. 6.15(a). Schematics for connections in DM and CM are provided in Fig. 6.15(b) and 6.15(c), respectively. Connections for CM are made in series, which increases the inductance by four times due to the doubled number of windings.

Figure 6.15: Experimental setup for the pulse test (a), differential-mode connections (b), and common-mode connection (c).

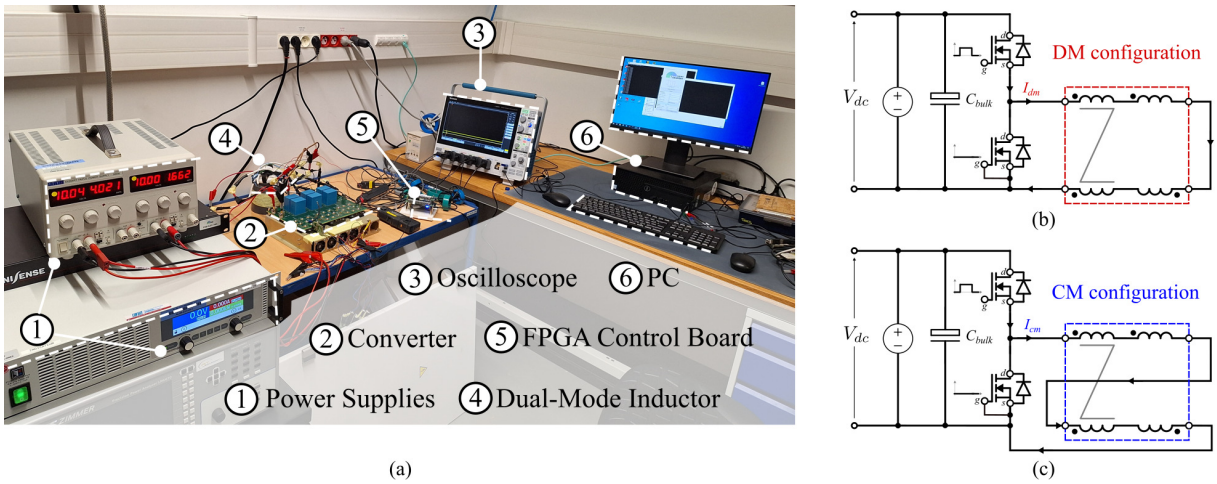

Source: Author.

Both discrete and integrated solutions will be tested, starting with the discrete inductors. Results are exhibited in Fig. 6.16.

From the DM test (graphs on the left), it is possible to see an inductance roll-off of about 21%, reaching a value of 53.7 µH at nominal current. For the common-mode, it is observed that the nanocrystalline core starts saturating at a current of about 0.35 A, reaching an inductance of 986 µH at this value.

Finally, the pulse tests were applied to the integrated inductor prototype and the graphs of Fig. 6.17 were obtained. Note that flux measurement probes were also added to all magnetic parts to monitor flux distribution and calculate saturation limits during the nominal operation point.

For differential-mode inductance, a roll-off of 18% occurred at nominal current and the inductance reached a value of 35 µH, very close to the value predicted by the optimization model of 37.7 µH. In common-mode, the nanocrystalline core starts to saturate at 2.0 A, reaching 1.1 T. However, since both DM and CM fluxes circulate within the

Figure 6.16: Pulse test results for the discrete inductors filter.

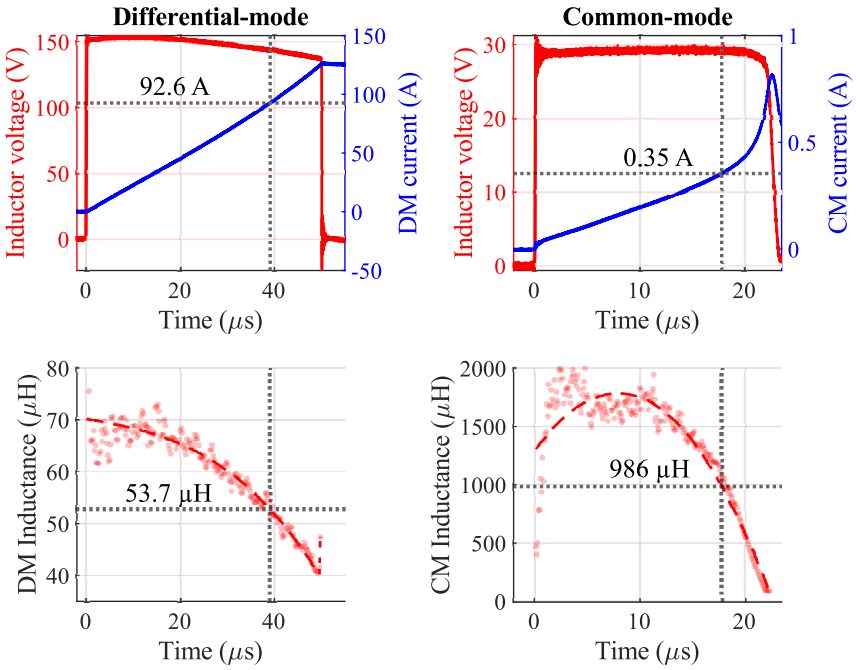

Source: Author.

Figure 6.17: Pulse test results for the Dual-Mode inductor prototype.

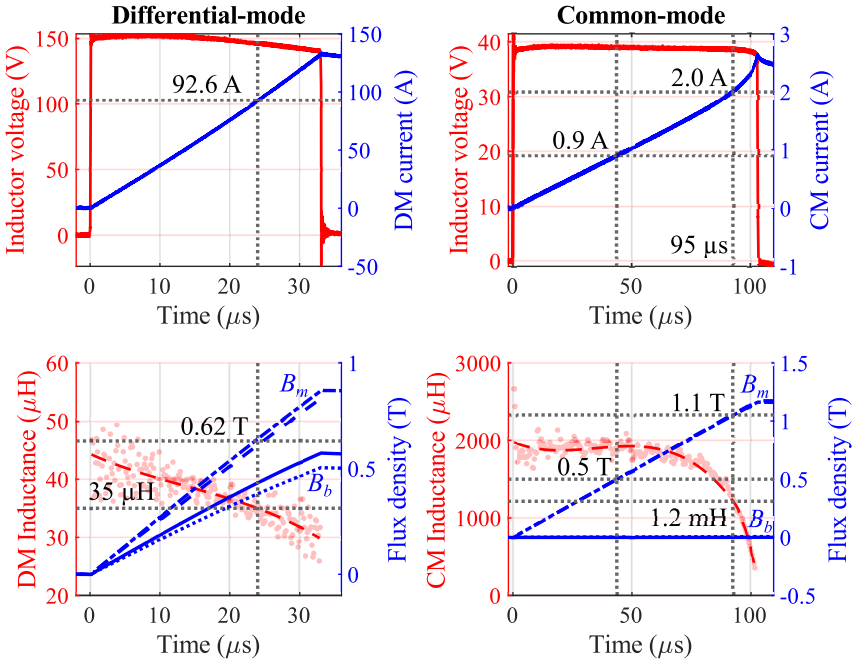

Source: Author.

toroidal core, the measured flux density in differential-mode at nominal current should be subtracted from the saturation flux density in common-mode to obtain the maximum allowed flux density variation in CM. In that regard, the maximum flux density in common-mode is 0.5 T, which corresponds to a CM current of 0.9 A, also very close to the design constraint provided to the optimization algorithm, therefore validating the model calculations. Table 6.5 shows comparisons between experimental results and design

parameters for DM and CM inductance of both inductor topologies.

Table 6.5: Comparison of obtained experimental results to model results.

Inductor topology	**DM inductance (μH)**		**CM inductance (μH)**	
	Model	*Measured*	*Model*	*Measured*
Discrete	35.4	53.7	300	307.5
Integrated	37.7	35	347.5	362.5

6.4 Chapter Conclusions

In this chapter, experimental tests were conducted to validate the developed analytical models for 2D and 3D air gap formulations that consider fringing flux effects and to verify the optimization results for the case study of an input filter for a 50kW Power Drive System.

The first set of tests consisted of validating the reluctance models. Experimental results were compared to 2D and 3D FEM simulations and indicated a maximum error of 6% to the experimental measurements and 3% in relation to the 3D FEM simulations. Experimental results also show that the model precisely predicts the saturation current, with an error of 1%. Nevertheless, the developed model has some limitations. The flux distribution test shows that the air gap lengths on each side can differ, resulting in flux imbalance inside the blocks of the leakage layer.

Experimental verification of the case study consisted of producing a prototype of the Dual-Mode inductor. The manufacturing involved some difficulties, such as the availability of materials such as XFlux 60µ on the desired geometry, fabrication of a special case with leakage layer openings and machining of the powder core blocks on the desired geometry. Regarding industrialization, these difficulties would be attenuated due to the high demand for specific core geometry and materials and a specific case production line. Therefore, the integrated inductor can be a viable solution to reduce weight and losses of EMI filters.

Tests performed in the prototype showed that the developed model was accurate, predicting DM and CM inductance values with errors of 7.2% and 4.3%, respectively. When compared to the discrete inductors, the Dual-Mode inductor presented a better performance in high-frequency due to the use of a low-permeability nanocrystalline core, and it was also saturated with a higher CM current in nominal operation.

Chapter 7

Conclusions and Future Work

7.1 General Conclusions

In the scope of this master thesis research, all the stablished objectives were achieved. Compact and viable solution for integrated CM/DM inductor was developed with the aid of a precise reluctance model and optimization routine. The work started by chosing an adequate leakage layer topology. The chosen one consists of two I-blocks crossing the CM choke sideways, which avoids orthogonal flux in the nanocrystalline tapes, thus reducing losses. Furthermore, this solution seemed to be the most compact and simple to fabricate.

In sequence, a precise analytical model was developed. An air-gap reluctance formulation that considers 3D fringing flux effects was used and led to much lower DM inductance calculation error when compared to other simpler methods. This model was then used in a multi-objective optimization routine to optimize the design of the integrated inductor aiming to reduce weight and losses while maximizing the DM inductance. The optimization algorithm was used in a case study to design a Dual-Mode inductor for a 50 kW Power Drive System input filter and compare its results to an optimized discrete solution. Optimization results showed significant reductions in weight and losses.

Experimental tests were conducted to validate the developed analytical models for the 2D and 3D air-gap formulations that consider fringing flux effects and to verify the optimization results for the case study of an input filter for a 50kW Power Drive System.

The first set of tests consisted of validating the reluctance models. Experimental results were compared to 2D and 3D FEM simulations and indicated a maximum error of 6% to the experimental measurements and 3% in relation to the 3D FEM simulations. Experimental results also showed that the model precisely predicts the saturation current, with an error of 1%. Nevertheless, the developed model has some limitations. The flux distribution test shows that the air-gap lengths on each side can differ, resulting in errors in the flux density inside the blocks of the leakage layer.

Experimental verification of the case study consisted of producing a prototype

of the Dual-Mode inductor. The manufacturing involved some difficulties, such as the availability of materials such as XFlux 60µ on the desired geometry, fabrication of a special case with leakage layer openings and machining of the powder core blocks on the desired geometry. Regarding industrialization, these difficulties would be attenuated due to the high demand for specific core geometry and materials and a specific case production line. Therefore, the integrated inductor can be a viable solution to reduce weight and losses of EMI filters.

The tests performed in the prototype showed that the developed model was accurate, predicting DM and CM inductance values with errors of 7.2% and 4.3%, respectively. When compared to the discrete inductors, the Dual-Mode inductor presented a better performance in high-frequency due to the use of a low-permeability nanocrystalline core, and it was also saturated with a higher CM current in nominal operation.

In conclusion, the developed work showed a great potential of the integrated CM/DM inductor to reduce weight and losses of EMI input filters. The prototype solution, despite being outperformed in DM inductance by the discrete solution, was a sub-optimal solution. In that sense, the Dual-Mode inductor would have lower losses and weight than the discrete solution with the most optimal materials for the leakage layer.

7.2 Future Work

For future work, it is proposed to extend the formulations for more complex applications, such as three-phase output EMI filters or On-board charger PFC input filters. In both cases, the flux waveforms are sinusoidal with high-frequency ripple in addition to the common-mode noise. Therefore, precise core loss and thermal models should be integrated to the optimization routine, besides the addition of a temperature rise constraint. Three-phase Dual-Mode chokes also have a much higher fabrication complexity, because the leakage layer would have to be in a star geometry and the winding distribution has to be optimized to guarantee maximum differential flux within the leakage paths.

Another important subject is the use of leakage layers in high-current applications (¿100 A), where multiple turns are not possible and the CM inductance is made of multiple cascaded passthrough cores on the bus bar. This solution, although having very low stray capacitance, compromises DM inductance, since there is almost no leakage due to the limited number of turns. Intercalating leakage layer blocks between the cascaded cores would contribute to an important DM inductance increase in these solutions.

A deeper analysis of EMI is also very important. This study showed a tradeoff between the increased CM inductance at high frequency due to the low permeability

nanocrystalline cores and the increase of parasitic capacitance because of the increase on the number of turns. In that regard, to optimize for EMI performance, it is necessary to model precisely the parasitic capacitances and core resistance to have an accurate impedance prediction. Comparative analysis of both solution during a power drive system operation are also important to verify CE attenuation.

Another topic is the development of a test setup to have common-mode and differential-mode currents in the device at the same time. With this, it would be possible to impose operation points of desired CM and DM fluxes in the magnetic parts and evaluate saturation behaviour and inductance roll-off of both inductances at the same time.

References

Balakrishnan, A., Joines, W., and Wilson, T. (1997). Air-gap reluctance and inductance calculations for magnetic circuits using a schwarz-christoffel transformation. *IEEE Transactions on Power Electronics*, 12(4):654–663.

Bashar, G., Frederic, P., and Thierry, W. (2016). New low μ nanocrystalline cores: An efficient way decreasing volume and mass. In *2016 18th European Conference on Power Electronics and Applications (EPE'16 ECCE Europe)*, pages 1–7.

Borsalani, J., Dastfan, A., and Ghalibafan, J. (2021). An integrated emi choke with improved dm inductance. *IEEE Transactions on Power Electronics*, 36(2):1646–1658.

Cao, Z., Chen, W., Shen, Z., Chen, Y., Jin, L., Ma, D., and Zou, B. (2022). A low loss orthogonal decoupling magnetic integrated structure for dual active bridge converter. *IEEE Transactions on Power Electronics*, 37(6):7013–7027.

Chen, C., Degner, M., and Liang, F. (2008). Inductor topologies with substantial common-mode and differential-mode inductance. Patent US 2008/0074227 A1.

Cougo, B. and Kolar, J. W. (2012). Integration of leakage inductance in tape wound core transformers for dual active bridge converters. In *2012 7th International Conference on Integrated Power Electronics Systems (CIPS)*, pages 1–6.

Cougo, B., Tuysüz, A., Mühlethaler, J., and Kolar, J. W. (2011). Increase of tape wound core losses due to interlamination short circuits and orthogonal flux components. In *IECON 2011 - 37th Annual Conference of the IEEE Industrial Electronics Society*, pages 1372–1377.

Dos Santos, V. (2019). *Modélisation des émissions conduites de mode commun d'une chaîne électromécanique. Optimisation paramétrique de l'ensemble convertisseur filtres sous contraintes CEM.* PhD thesis, Université de Toulouse, Institut National Polytechnique de Toulouse.

EASA (2022). European aviation environmental report 2022. Technical report, European Union Aviation Safety Agency.

European Parliament, C. o. t. E. U. (2024). Regulation (eu) 2024/1735 of the european parliament and of the council of 13 june 2024 on establishing a framework of measures

for strengthening europe's net-zero technology manufacturing ecosystem and amending regulation (eu) 2018/1724 (text with eea relevance).

Gao, S. and Zhao, Z. (2021). Magnetic integrated llc resonant converter based on independent inductance winding. *IEEE Access*, 9:660–672.

Hoffmann Sathler, H. (2021). *Optimization of GaN-based Series-Parallel Multilevel Three-Phase Inverter for Aircraft applications*. Theses, Université Paris-Saclay.

IPCC (2023). Climate change 2023: Synthesis report. contribution of working groups i, ii and iii to the sixth assessment report of the intergovernmental panel on climate change. Technical report, IPCC, Geneva, Switzerland.

Kacki, M., Rylko, M. S., Hayes, J. G., and Sullivan, C. R. (2017). Magnetic material selection for emi filters. In *2017 IEEE Energy Conversion Congress and Exposition (ECCE)*, pages 2350–2356.

Lai, R., Maillet, Y., Wang, F., Wang, S., Burgos, R., and Boroyevich, D. (2010). An integrated emi choke for differential-mode and common-mode noise suppression. *IEEE Transactions on Power Electronics*, 25(3):539–544.

Lutz, M. and Wright, N. (2006). *Explanation and experiences with RTCA/DO160 Level 5 avionics testing*. EMC Partner AG.

Magnetics-Inc. (2021). Magnetics ferrite catalog. Technical report, Magnetics Inc.

Mühlethaler, J. (2012). *Modeling and Multi-Objective Optimization of Inductive Power Components*. PhD thesis, ETH Zurich.

Mühlethaler, J., Kolar, J. W., and Ecklebe, A. (2011). A novel approach for 3d air gap reluctance calculations. In *8th International Conference on Power Electronics - ECCE Asia*, pages 446–452.

Nikolov, G. T. and Valchev, V. C. (2009). Nanocrystalline magnetic materials versus ferrites in power electronics. *Procedia Earth and Planetary Science*, 1(1):1357–1361. special issue title: Proceedings of the International Conference on Mining Science & Technology (ICMST2009).

Pavlovsky, M., de Haan, S. W. H., and Ferreira, J. A. (2006). Winding losses in high-current, high-frequency transformer foil windings with leakage layer. In *2006 37th IEEE Power Electronics Specialists Conference*, pages 1–7.

Rodriguez-Sotelo, D., Rodriguez-Licea, M. A., Soriano-Sanchez, A. G., Espinosa-Calderon, A., and Perez-Pinal, F. J. (2020). Advanced ferromagnetic materials in power electronic converters: A state of the art. *IEEE Access*, 8:56238–56252.

Rylko, M. S., Hartnett, K. J., Hayes, J. G., and Egan, M. G. (2009). Magnetic material selection for high power high frequency inductors in dc-dc converters. In *2009 Twenty-Fourth Annual IEEE Applied Power Electronics Conference and Exposition*, pages 2043–2049.

Sclocchi, M. (2010). Input filter design for switching power supplies. Technical report, National Semiconductor Corporation.

Shudarek, T. A. (2009). Common mode, differential mode three phase inductor. Patent US 2009/0261939 A1.

Singh, S., Dwiza, B., Jayaraman, K., and Mishra, P. (2024). Novel single-stage and two-stage integrated magnetic chokes for dc-side emi filter in motor drive applications. *IEEE Transactions on Power Electronics*, 39(1):570–581.

Tan, W., Cuellar, C., Margueron, X., and Idir, N. (2013). A common-mode choke using toroid-eq mixed structure. *IEEE Transactions on Power Electronics*, 28(1):31–35.

Upadhyay, A. K. (1994). Integrated common mode and differential mode inductor device. Patent US 1994/005313176 A.

Vacuumschmelze (2016). Emc products based on nanocrystalline vitroperm. Technical report, Vacuumschmelze.

Wang, S., Yuan, D., Wang, A., Liu, K., Li, H., and Wang, S. (2019). Circuit-field coupling and magnetic-thermal coupling analysis of rrf converter designed with magnetic integration. *IEEE Transactions on Magnetics*, 55(5):1–8.

Wright, N. and Lutz, M. (2006). Developments in the field of avionics testing equipment. In *2006 9th International Conference on Electromagnetic Interference and Compatibility (INCEMIC 2006)*, pages 242–249.

WSDOT (2019). Electric aircraft working group report. Technical report, WSDOT.

Zhang, B. and Wang, S. (2020). A survey of emi research in power electronics systems with wide-bandgap semiconductor devices. *IEEE Journal of Emerging and Selected Topics in Power Electronics*, 8(1):626–643.

Appendix A

Mechanical Parametrization and Automated 3D Modeling of the Dual-Mode Inductor

In this appendix, the mechanical description of the Dual-Mode inductor will be detailed, as well as the process of automation of 3D modeling for faster FEM simulations.

A.1 Mechanical parametrization

To cover all possible core geometries, an oblong (or stadium) core will be considered for generalization and toroidal cores are only a particular case of the oblong geometry. In that regard, consider the geometric scheme of Fig. A.1.

The figure represents the oblong core with leakage layer block. The desired parameters to be used in the optimization routine are the air gap area A_g, for reluctance calculation, and the window area A_w, for winding feasibility calculation.

The oblong core has two internal and two external radii, ID_1,ID_2,OD_1 and OD_2. In a toroidal core, $ID_1 = ID_2$ and $OD_1 = OD_2$ and the variable l_{mh} would be zero. In that sense, we can describe the highlighted lengths and angles in terms of the oblong and I-block core parameters as follows

$$l_{mh} = ID_1 - ID_2 \qquad w_m = \frac{OD_2 - ID_2}{2} \qquad x = \frac{l_b - l_{mh}}{2} \tag{A.1}$$

$$x = \frac{w_b - l_{mh}}{2} \qquad r_o = \frac{OD_2}{2} \qquad r_i = \frac{ID_2}{2} \tag{A.2}$$

$$\sin\alpha = \frac{x}{r_o} \longrightarrow \alpha = \arcsin\left(\frac{w_b - l_{mh}}{OD_2}\right) \tag{A.3}$$

Figure A.1: Mechanical parameters of the Dual-Mode inductor.

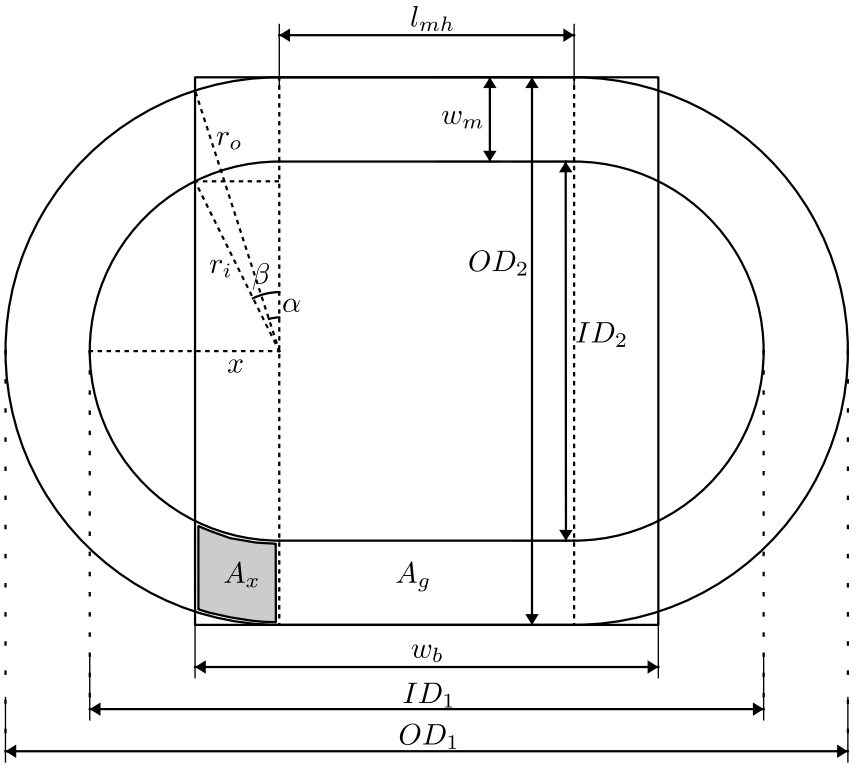

Source: Author.

$$\sin\beta = \frac{x}{r_i} \longrightarrow \beta = \arcsin\left(\frac{w_b - l_{mh}}{ID_2}\right) \tag{A.4}$$

With that, we can determine the area A_x, which is the contact area of the block and a circular halve of the oblong core.

$$A_x = \int_{r_i}^{r_o}\int_{0}^{\alpha} r\, d\theta\, dr + x \cdot r_o \sin\left(\frac{\pi}{2} - \alpha\right) - x \cdot r_i \sin\left(\frac{\pi}{2} - \beta\right) - \int_{0}^{r_i}\int_{\alpha}^{\beta} r\, d\theta\, dr \tag{A.5}$$

$$A_x = \frac{r_o^2 - r_i^2}{2} \cdot \alpha + \frac{x}{2} \cdot r_o \cos\alpha - \frac{x}{2} \cdot r_i \cos\beta - \frac{r_i^2}{2} \cdot (\beta - \alpha) \tag{A.6}$$

Then, the air gap area A_g can be obtained as follows

$$A_g = 2A_x + l_{mh} w_m \tag{A.7}$$

The window area can be described as

$$A_w = \int_{0}^{r_i}\int_{\beta}^{\pi-\beta} r\, d\theta\, dr - 2 \cdot \frac{x \cdot r_i \cos\beta}{2} \tag{A.8}$$

$$A_w = \frac{r_i^2(\pi - 2\beta)}{2} - 2 \cdot \frac{x \cdot r_i \cos\beta}{2} \tag{A.9}$$

A.2 3D modeling and winding parametrization

This work comprises model validation that involves three-dimensional effects such as air gap flux fringing effects, making it necessary to use 3D Finite Element Analysis software. However, multi-objective optimization routines find a large number of solutions and validating them in FEM software can take a lot of work to model the inductor geometry. With that in mind, a Python script was developed to serve as a macro in the 3D modeling software FreeCAD for creating a 3D model of a desired solution.

The magnetic cores can be easily parametrized with the variables shown in Fig. A.1 with the addition of the heights of both nanocrystalline and iron powder blocks. However, to model the windings, it is necessary to parametrize a helix wrapped around a toroidal core. Fig. A.2 shows how a period of a wrapped helix can be obtained as function of the core and winding parameters.

Figure A.2: Parametrization of a winding guide helix.

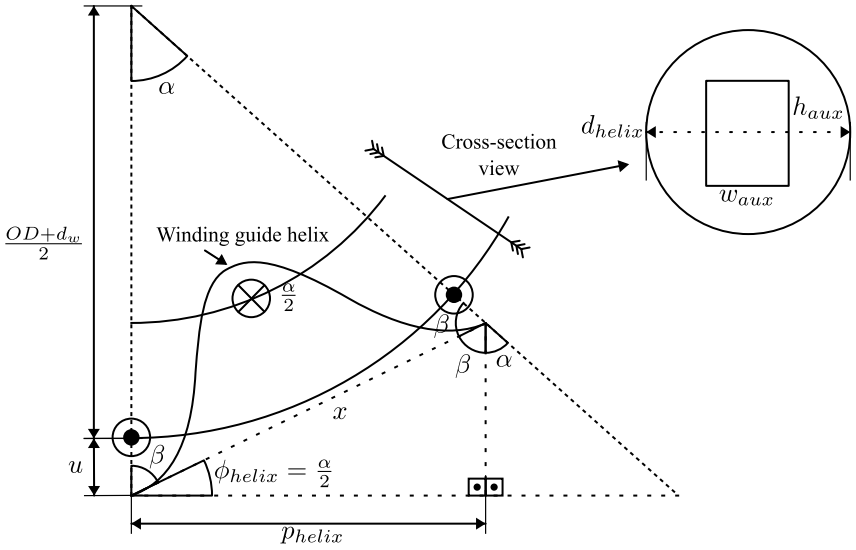

Source: Author.

The helix has the parameters of a pitch p_{helix} and an angle $\phi_{helix} = \frac{\alpha}{2}$, where α is the angle between two consecutive turns. In that sense, if one winding of the inductor has an angular span θ, we can derive the helix parameters as follows

$$\alpha = \frac{\theta}{N_m} \qquad \beta = \frac{\pi - \alpha}{2} \tag{A.10}$$

The helix has to wrap around the toroidal core, therefore its diameter d_{helix} must be larger than the diagonal of the core cross-section. In that regard, we add a multiplier to this value to obtain the following

$$u = 1.2 \cdot \frac{\sqrt{w_{aux}^2 + h_{aux}^2}}{2} - \frac{w_{aux}}{2} \tag{A.11}$$

$$x = \frac{\sin\alpha}{\sin\beta} \cdot \left(\frac{OD + d_w}{2} + u \right) \tag{A.12}$$

$$d_{helix} = 2\left(u + \frac{w_{aux}}{2} \right) \tag{A.13}$$

$$p_{helix} = x \cos\left(\frac{\alpha}{2} \right) \tag{A.14}$$

With that, we have a winding guide helix to make a complete turn. With subsequent boolean operations of the modeling software, it is possible to make the winding around the toroidal core. With this, the inductor can be completely parametrized by extending these formulations to multiple and parallel windings.

Therefore, the FEM simulation process of an inductor solution would be identifying the solution on the optimization solution graph and pick the solution ID and the corresponding string to insert it to the FreeCAD script. This model can then be exported to the 3D-FEM software and simulated. Fig. A.3 shows an example of a solution datatip and Fig. A.4 shows the FreeCAD window after loading a solution string.

Figure A.3: Optimization solution graph with a detailed solution datatip.

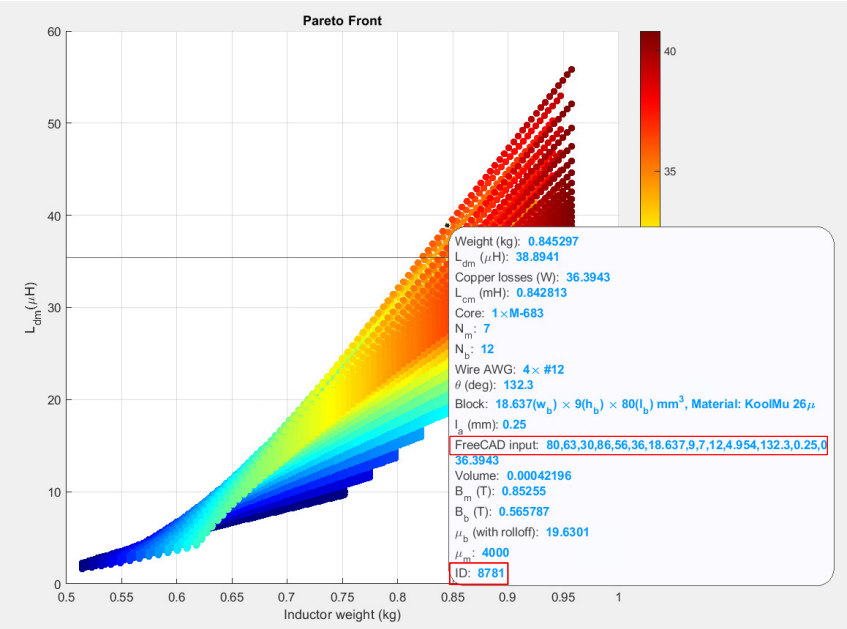

Source: Author.

Figure A.4: Automated 3D modeling of an integrated inductor solution.

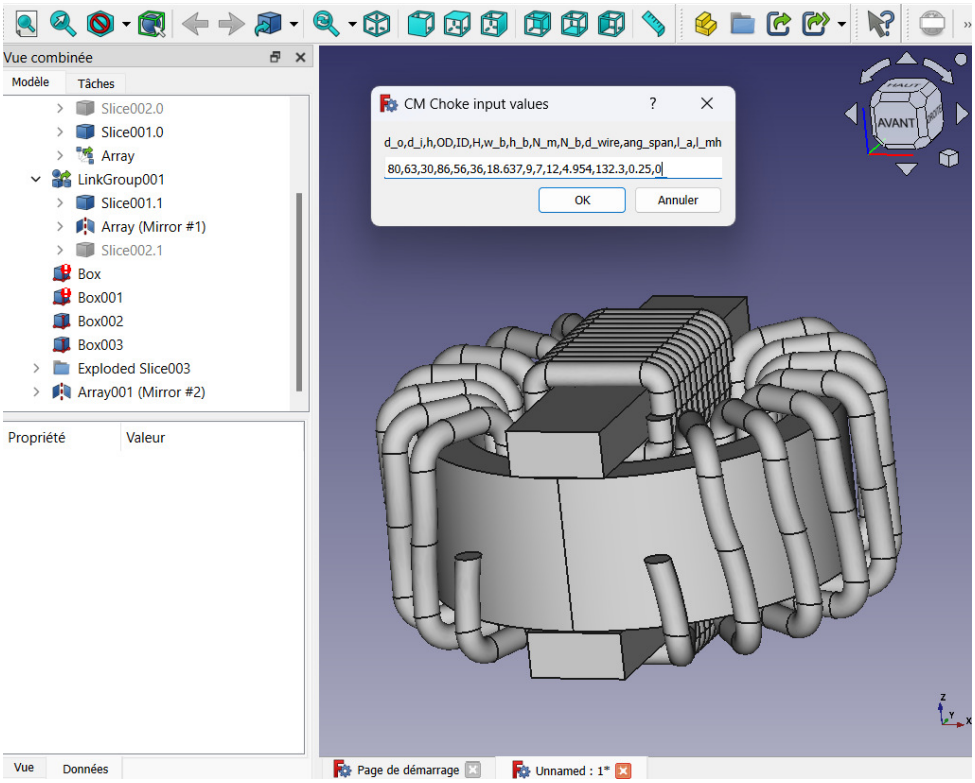

Source: Author.